AGU PUBLICATIONS

JGR

Journal of Geophysical Research: Atmospheres

RESEARCH ARTICLE

10.1002/2016JD024775

Evaluating Arctic cloud radiative effects simulated by NICAM with A-train

Tempei Hashino[1,2], Masaki Satoh[1], Yuichiro Hagihara[2], Seiji Kato[3], Takuji Kubota[4], Toshihisa Matsui[5], Tomoe Nasuno[6], Hajime Okamoto[2], and Miho Sekiguchi[7]

[1]Atmosphere and Ocean Research Institute, The University of Tokyo, Kashiwa, Japan, [2]Now at Research Institute for Applied Mechanics, Kyushu University, Fukuoka, Japan, [3]NASA Langley Research Center, Hampton, Virginia, USA, [4]Japan Aerospace Exploration Agency, Tsukuba, Japan, [5]NASA Goddard Space Flight Center, Greenbelt, Maryland, USA, [6]Japan Agency for Marine-Earth Science and Technology, Yokohama, Japan, [7]Tokyo University of Marine Science and Technology, Tokyo, Japan

Key Points:
- Cloud albedo/shading and greenhouse effects of NICAM were underestimated compared with A-train data
- The biases can be connected to cloud microphysics and cloud types
- Too frequent and too thin high clouds partially compensate for lack of supercooled water clouds

Supporting Information:
- Supporting Information S1

Correspondence to:
T. Hashino,
hashino@riam.kyushu-u.ac.jp

Citation:
Hashino, T., M. Satoh, Y. Hagihara, S. Kato, T. Kubota, T. Matsui, T. Nasuno, H. Okamoto, and M. Sekiguchi (2016), Evaluating Arctic cloud radiative effects simulated by NICAM with A-train, *J. Geophys. Res. Atmos.*, *121*, 7041–7063, doi:10.1002/2016JD024775.

Received 12 JAN 2016
Accepted 27 MAY 2016
Accepted article online 2 JUN 2016
Published online 18 JUN 2016

Abstract Evaluation of cloud radiative effects (CREs) in global atmospheric models is of vital importance to reduce uncertainties in weather forecasting and future climate projection. In this paper, we describe an effective way to evaluate CREs from a 3.5 km mesh global nonhydrostatic model by comparing it against A-train satellite data. The model is the Nonhydrostatic Icosahedral Atmospheric Model (NICAM), and its output is run through a satellite-sensor simulator (Joint Simulator for satellite sensors) to produce the equivalent CloudSat radar, CALIPSO lidar, and Aqua Clouds and the Earth's Radiant Energy System (CERES) data. These simulated observations are then compared to real observations from the satellites. We focus on the Arctic, which is a region experiencing rapid climate change over various surface types. The NICAM simulation significantly overestimates the shortwave CREs at top of atmosphere and surface as large as 24 W m^{-2} for the month of June. The CREs were decomposed into cloud fractions and footprint CREs of cloud types that are defined based on the CloudSat-CALIPSO cloud top temperature and maximum radar reflectivity. It turned out that the simulation underestimates the cloud fraction and optical thickness of mixed-phase clouds due to predicting too little supercooled liquid and predicting overly large snow particles with too little mass content. This bias was partially offset by predicting too many optically thin high clouds. Offline sensitivity experiments, where cloud microphysical parameters, surface albedo, and single scattering parameters are varied, support the diagnosis. Aerosol radiative effects and nonspherical single scattering of ice particles should be introduced into the NICAM broadband calculation for further improvement.

1. Introduction

The Arctic has experienced rapid warming since the middle twentieth century [*Intergovernmental Panel on Climate Change,* 2013]. A recent study shows that recent cold winters in Eurasian continent are attributed to reduction of sea ice due to the warming and subsequent formation of blocking patterns [*Mori et al.,* 2014]. The Arctic clouds modulate the surface energy budget by scattering shortwave (SW) radiation and absorbing/emitting the longwave (LW) radiation, affecting the ice sheet and sea ice extent [e.g., *Curry et al.,* 1996; *Kay and Gettelman*, 2009]. According to another study, low-level liquid clouds, optically thick enough to increase the downward LW radiation yet still allow SW to melt the surface, contributed to the extensive melting of Greenland ice sheets in July 2012 [*Bennartz et al.,* 2013]. Arctic mixed-phase boundary layer clouds are particularly important because they have a greater optical thickness than ice-only clouds and ubiquitous [e.g., *Shupe and Intrieri,* 2004; *de Boer et al.,* 2009] yet are not well simulated by numerical models [e.g., *Morrison et al.,* 2011; *Cesana et al.,* 2012; *de Boer et al.,* 2012]. *Gettelman et al.* [2010] reported that surface radiative fluxes in the Arctic region are particularly sensitive to changes in the parameterization of ice clouds in a global circulation model. Therefore, it is crucial to establish a framework to evaluate/understand cloud radiative effects (CREs) in terms of cloud types including the phase of hydrometeors.

In addition to retrieving geophysical parameters, advances in satellite-based global observation are vitally important for evaluating simulated clouds. The A-train of satellite constellation provides high-resolution polar-orbit data with multifrequency, multiplatform instruments [*L'Ecuyer and Jiang,* 2010]. The active sensors, CloudSat Cloud Profiling Radar (CPR) and the Cloud-Aerosol Lidar and Infrared Pathfinder Satellite Observation (CALIPSO) Cloud-Aerosol Lidar with Orthogonal Polarization (CALIOP), play a central role in the model evaluation because they directly measure the vertical profile of backscattering from cloud and precipitating particles [e.g., *Chepfer et al.,* 2008; *Su et al.,* 2013; *Suzuki et al.,* 2013]. Use of Aqua Clouds and the Earth's Radiant Energy

System (CERES) [*Wielicki et al.,* 1996] from the A-train sheds light on the characteristics of single and multiple-layer clouds in terms of CREs [*Li et al.,* 2011]. *Nam et al.* [2012] evaluated clouds and CREs in the Tropics simulated by the fifth phase of the Coupled Model Intercomparison Project (CMIP5) general circulation models (GCMs) with CALIPSO CALIOP, Polarization and Anisotropy of Reflectances for Atmospheric Sciences coupled with Observations from a Lidar (PARASOL) monodirectional reflectance, and CERES radiative fluxes at top of atmosphere (TOA). They show that the GCMs predict low clouds that are optically too thick and too few yet predict too many middle and high clouds above the low clouds. *Greenwald et al.* [2010] evaluated the radiative heating profiles simulated by The Weather Research and Forecasting (WRF) Model [*Skamarock et al.,* 2005] with the Level 2 flux and heating rate products (2B-FLXHR) [*L'Ecuyer et al.,* 2008] and found that net CREs at TOA, at surface and for the atmosphere are simulated better for cirrus and low-level cloud regime than for the other regimes. Therefore, it is now possible to understand not only the biases of the radiative fluxes over a specific domain at TOA but also the compensating errors among various cloud types in the simulated CREs.

The aims of this paper are (1) to evaluate Arctic CREs simulated by a global cloud-resolving model, the nonhydrostatic icosahedral atmospheric model (NICAM) [*Tomita and Satoh,* 2004; *Satoh et al.,* 2008, 2014] and (2) to propose a way to evaluate simulated CREs over inhomogeneous surface cover with an understanding of both the simulated cloud types and cloud microphysics. This study exploits the data from A-train CloudSat CPR, CALIPSO CALIOP, and Aqua CERES. To facilitate the characterization of CREs and cloud microphysics, we introduce a simple cloud-type scheme that is based on cloud top temperatures and lidar-radar signals. This is similar to the previous work by *Webb et al.* [2001], where the International Satellite Cloud Climatology Project (ISCCP) [*Rossow and Schiffer*, 1991] was combined with the Earth Radiation Budget Experiment (ERBE). This paper advances the approach by using a cloud particle type retrieval product to clarify the dependence of CREs on the phase of hydrometeors from the space for the first time and attempts to link the biases in CREs to those in cloud microphysics. The joint ESA/JAXA Earth Clouds and Radiation Explorer (EarthCARE) mission [*Gelsthorpe et al.,* 2008; *Kimura et al.,* 2010; *Illingworth et al.,* 2014] will have a cloud radar with Doppler measurement, a high spectral resolution lidar, a multispectral imager, and a broadband radiometer, which is expected to take over the observation of CloudSat and CALIPSO. The approach proposed in this study can be directly applied to observations of EarthCARE satellite.

The observation and simulation data sets are described in section 2 along with definition of CREs and description of the cloud-type diagram using CloudSat CPR and CALIPSO CALIOP signals. In section 3 domain-averaged fluxes and the relation to cloud microphysics are analyzed in detail with use of the cloud type. Then, section 4 presents sensitivities of the simulated signals to cloud microphysical parameters assumed, surface albedo, and single scattering parameters of nonspherical ice particles. Finally, section 5 summarizes the major findings and lists future tasks. For symbols and acronyms used in this paper, see Table 1.

2. Data Sets and Methodology

2.1. CloudSat-CALIPSO Merged Data Set

The observational data set used in this study is the CloudSat-CALIPSO merged data set (CSCA-MD) [*Hagihara et al.,* 2010]. The CSCA-MD consists of the observables and cloud products derived from CloudSat and CALIPSO. The observable product (hereafter Kyushu University observables; KU-obs) contains colocated CALIOP 532 and 1064 nm attenuated backscattering coefficients and the CPR 94-GHz radar reflectivity. The horizontal and vertical resolutions are 1100 and 240 m, respectively. The altitude of the grid centers ranges from 120 to 19800 m. The cloud products include algorithm-retrieved cloud masks (KU-mask) [*Hagihara et al.,* 2010], vertically resolved cloud particle type (KU-type) [*Yoshida et al.,* 2010; *Hirakata et al.,* 2014], and cloud microphysics (KU-micro) [*Okamoto et al.,* 2010]. From the radar and lidar signals, four cloud masks (C1–C4) are produced. C1 is a radar-only scheme based on the CPR level 2B-GEOPROF cloud mask (release R04), whereas C2 uses a lidar-only approach in which a threshold and spatial-continuity test is applied to CALIPSO lidar level 1B (version 3.01). *Hagihara et al.* [2010] showed that our cloud mask results had less contamination by remaining noise or aerosol signals compared with those of the CALIPSO standard cloud mask, the CALIPSO Lidar Level 2 Vertical Feature Mask (VFM) version 2 [*Vaughan et al.,* 2009; *Liu et al.,* 2009]. The overestimation of the cloud fraction in the VFM version 3 was also reported in *Hagihara et al.* [2014]. From C1 and C2 regions, we define C3 regions as their intersection and C4 regions as their union. The KU-type uses the depolarization ratio and the ratio of attenuated backscattering coefficient of two successive layers in

Table 1. Symbols and Acronyms

Name	Description
AE	aerosol radiative (direct) element
α_s	surface albedo
BE	beam convolution effect
BETTER	beta-temperature radar-conditioned diagram
β_{532}	532 nm lidar backscattering coefficient (1/m/str)
COT	cloud optical thickness
CRE	cloud radiative effect
CE	cloud radiative element
CRE_i and CE_i	cloud radiative effect and cloud radiative element of cloud type *i* ($i = 1,\ldots,10$)
$\cos\theta_0$	cosine of solar zenith angle
CTT	cloud top temperature (°C)
C1	cloud mask detected by radar
C2	cloud mask detected by lidar
C3	cloud mask detected both by radar and lidar
C4	cloud mask detected either by radar or lidar
F	broadband flux
F_{cloudy}	overcast broadband flux, fully covered with clouds
F_{clear}	clear-sky broadband flux
$F_{cloud\text{-}free}$	broadband flux under overcast sky with clouds removed
F_{all}	all-sky broadband flux, weighted average of F_{clear} and F_{cloudy}.
$F_{no\text{-}cloud}$	broadband flux without clouds, weighted average of F_{clear} and $F_{cloud\text{-}free}$
↑, ↓	upward, downward radiation
IWC	ice water content
LW	longwave
N, N_i	cloud fraction, cloud fraction of cloud type *i*
PDF	probability density function
R_{eff}	effective radius
$R_{eff,m}$	mass-equivalent effective radius
SFC	surface
SW	shortwave
T	Air temperature
TOA	top of atmosphere
Z_e	94 GHz radar reflectivity (dBZ)
Z_{mx}	maximum radar reflectivity of a cloud layer or a single profile (dBZ)

vertical to infer vertically resolved cloud particle type such as warm water, supercooled water, randomly oriented ice or horizontally oriented ice, and mixture of ice and water [*Yoshida et al.,* 2010]. See *Hashino et al.* [2013] for more details about this data set.

To this data set, we add the broadband flux observations from CERES-MODIS-CALIPSO-CloudSat (CCCM) data set. The CERES instrument has three channels, a SW channel (0.3–5.0 μm), a window channel (8–12 μm), and a total channel (0.3 to more than 200 μm), that all measure TOA spectrum radiances. The radiances are then converted to fluxes using the empirical angular distribution models in *Loeb et al.* [2003a, 2003b].

In addition to the TOA fluxes, the CCCM product provides computed surface fluxes at the instantaneous footprint level [*Kato et al.,* 2010, 2011]. In the enhanced surface flux scheme, active sensor-derived properties are first chosen for computation of the irradiance, followed by an enhanced CERES cloud algorithm. In the algorithm the cloud and aerosol properties derived from the CERES cloud algorithm are combined with the cloud height and cloud masks derived from CALIPSO and CloudSat, cloud properties derived from CALIPSO and CloudSat, and aerosol properties derived from CALIPSO. The spectral albedos are derived from MCD43C1 Climate Modeling Grid BRDF/Albedo Model Parameters Product over land. The resulting surface fluxes are constrained by CERES-derived TOA fluxes through use of 1-D radiative transfer theory. *Kato et al.* [2013] report that the monthly downward surface irradiances over ocean (land) have biases of 4.7 and $-2.5\,\mathrm{W\,m^{-2}}$ (-1.7 and $-1.0\,\mathrm{W\,m^{-2}}$) for SW and LW, respectively, and RMS differences of 13.3 and $7.1\,\mathrm{W\,m^{-2}}$ (7.8 and $7.6\,\mathrm{W\,m^{-2}}$), compared to ground observation. The monthly zonal uncertainties of the downward SW and LW fluxes due to uncertainties in aerosol, clouds, and others are about 8 and $10\,\mathrm{W\,m^{-2}}$ over ocean, and 10 and $15\,\mathrm{W\,m^{-2}}$ over land (see their Table 5 and 6). The resulting surface irradiance estimates were significantly improved, especially over polar regions, compared to a previous passive sensor-only product [see *Kato et al.*, 2011, Figure 10].

To colocate the CCCM product, we simply assign the CERES footprint that is closest to each CSCA-MD grid point. As the horizontal footprint size of CERES is about 20 km, the closest CCCM grid point has to be within 10 km distance. Otherwise, no CCCM data are assigned for the CSCA-MD grid point. As the horizontal resolution of the CSCA-MD is 1.1 km, one CERES footprint sample may be shared by up to about 18 CSCA-MD samples. Thus, the irradiance of a single CERES footprint includes clear-sky and cloudy profiles detected by the active sensors.

2.2. NICAM—Joint Simulator Data Set

The NICAM simulation is a 3.5 km mesh global simulation implemented from 00 Z of 15 June to 00 Z of 25 June in 2008. The vertical grid resolution is stretched from 162 m at the surface to about 3 km at the model top (~40 km above sea level). See *Hashino et al.* [2013] for the details of the data set. NICAM can be used as a global cloud-resolving model that explicitly simulates convection and associated cloud-precipitation systems with a grid-resolved scale [*Miyamoto et al.,* 2013]. The 3.5 km mesh scale allows us to compare the simulated signals from each vertical profile directly with footprint observations from satellites. The cloud microphysical scheme is a single-moment bulk parameterization called NICAM Single-moment Water 6 (NSW6), which puts hydrometeors into the categories of cloud water, rain, cloud ice, snow, and graupel [*Tomita,* 2008]. It is important to note that the assumption in NSW6, such as parameters of particle size distribution, bulk density of ice particles, and effective radius, was reflected in the forward simulation of signals [see *Hashino et al.,* 2013].

The A-train satellite signals are simulated from the NICAM output using the Joint Simulator for Satellite Sensors (Joint Simulator), which is developed under the EarthCARE mission. The 94 GHz radar reflectivity and 532 nm lidar backscatters are simulated with the EarthCARE Active Sensor simulator (EASE) [*Okamoto et al.,* 2003, 2007, 2008; *Nishizawa et al.,* 2008]. Then, the four cloud masks (C1–C4) are generated from the simulated radar and lidar signals [see *Hashino et al.,* 2013, for more details]. The hardware-related noises in observed lidar backscatters are sufficiently removed during C2 process [*Hagihara et al.,* 2010], and therefore, the simulator does not need to simulate the noises for model evaluation.

For this study, the broadband fluxes corresponding to the Aqua CERES observation were calculated with a broadband simulator within the Joint Simulator, which is based on MSTRN-X [*Sekiguchi and Nakajima,* 2008]. MSTRN-X is also run in the NICAM simulation to obtain radiative flux and heating rate profiles. It uses the two-stream approximation and correlated-*k* distribution method to estimate the gas absorption. To obtain sample volumes consistent with CERES, we simulated the signals directly from the 3.5 km mesh data and then horizontally averaged the grid-level signals using a Gaussian beam convolution technique [*Masunaga and Kummerow,* 2005]. This way, contribution from clear sky and cloud within a CERES footprint is taken into account. Note that all the categories of hydrometeors in NSW6 were included for this offline calculation although the online calculation included only cloud water and cloud ice. This is necessary in order to achieve consistency among signal diagnoses since other signals were calculated with all the categories included.

The nonspherical scattering of ice particles is one of the major sources of uncertainty in simulating broadband fluxes as well as radar and lidar signals. Impacts of the nonsphericity on the active sensors were discussed in *Hashino et al.* [2013] for this data set, and it turned out that the cloud microphysical diagnosis was robust in a qualitative sense due to the large model-observation differences. *Seiki et al.* [2014] evaluated the vertical profiles of LW and SW fluxes simulated with NICAM and the two-moment scheme called NDW6 [*Seiki and Nakajima*, 2014]. Although midlatitude cirrus clouds with optical thickness of about six were their target, the use of nonspherical single scattering parameters led to about 60 W m^{-2} decrease in SW downward fluxes at surface and about 100 W m^{-2} increase in SW upward fluxes at 16 km from the Mie approximation. In order to quantify the uncertainty associated with assumed ice habits, a spectrally consistent single-scattering data set developed by *Yang et al.* [2013] was incorporated into Joint Simulator. In the sensitivity test shown below, as done in *Hashino et al.* [2013], one ice habit is applied to all the three categories of ice in NSW6 to obtain the maximum range of uncertainty.

2.3. Definition of Cloud Radiative Effects

For a specific domain, the CRE at TOA (W m^{-2}) is typically defined as the difference between the flux with a clear-sky flux (F_{clear}) and the flux with clouds partially or fully covering the domain (F_{all}):

$$\mathrm{CRE} = F_{\mathrm{clear}} - F_{\mathrm{all}}. \tag{1}$$

$F_{\rm all}$ is defined as

$$F_{\rm all} = (1 - N)F_{\rm clear} + NF_{\rm cloudy}, \tag{2}$$

where $F_{\rm cloudy}$ is the flux from grids with clouds fully covering and N is the cloud fraction in the domain. Now consider a grid box fully covered by clouds. We can calculate a flux for the grid without the clouds, which is denoted as $F_{\text{cloud-free}}$. Then, we introduce an average flux over the domain with clouds removed from the fully cloudy grids ($F_{\text{no-cloud}}$):

$$F_{\text{no-cloud}} = (1 - N)F_{\rm clear} + NF_{\text{cloud-free}}. \tag{3}$$

By replacing $F_{\rm clear}$ with $F_{\text{no-cloud}}$ in equation (1) for both observation and simulation, the CRE can be defined as a product of cloud fraction N and cloud radiative element CE:

$$\mathrm{CRE} = N\cdot\mathrm{CE} = N\cdot\left(F_{\text{cloud-free}} - F_{\rm cloudy}\right). \tag{4}$$

Previous studies [*Allan and Ringer,* 2003; *Sohn and Bennartz,* 2008; *Sohn et al.,* 2010] showed that the clear-sky atmosphere is usually drier than the cloudy atmosphere nearby, and therefore, the LW $F_{\rm clear}$ tends to be larger than the LW $F_{\text{cloud-free}}$. In the above definition the differences in water vapor and temperature between clear and cloudy sky conditions are removed from CREs. For the simulation, the CE is computed for each grid box since NICAM takes 0 or 1 of cloud fraction in a box. $F_{\text{cloud-free}}$ is calculated simply by ignoring hydrometeors from the cloudy grids and by MSTRN-X. As for the observation, the CE is defined for instantaneous footprint samples of CSCA-MD. The CCCM-enhanced product includes the TOA and surface irradiances computed without aerosol and clouds, which is assigned to $F_{\text{cloud-free}}$. Aerosol is not included in calculation of $F_{\text{cloud-free}}$ because the simulation does not have aerosol information. In other words, the CE for overcast grids includes effects of both clouds and aerosol particles for the observation but only clouds for the simulation. The CE for clear-sky samples (no clouds) can be also calculated with use of the cloud masks.

2.4. Adjustment of Fluxes for Averaging

The SW CREs constitute valuable information to evaluate cloud optical properties. The importance of the SW arises because, compared to the LW, (1) clouds do not become optically opaque in the SW until higher values of liquid water path are reached [*Shupe and Intrieri,* 2004] and (2) the SW broadband is more sensitive to the effective radius and number concentration of ice particles [e.g, *Seiki et al.,* 2014]. *Shupe and Intrieri* [2004] introduced a simple radiative transfer model for the shortwave net cloud radiative effect at surface ($\mathrm{CRE}_{\rm SW,SFC}$). For overcast sky, it is

$$\mathrm{CRE}_{\rm SW,SFC} \approx t_{bs} S\cos\theta_0 (1 - \alpha_s)(t_{cs} - 1), \tag{5}$$

where t_{bs} is the broadband atmospheric SW transmittance, S is the solar constant, $\cos\theta_0$ is the cosine of solar zenith angle, α_s is the broadband surface albedo, and t_{cs} is the broadband cloud SW transmittance. Our main interest is to evaluate the simulated t_{cs}. The model indicates that evaluation of CREs over the various land covers of the Arctic is challenging for the SW CREs due to model-observation differences in surface albedo. In addition, the solar zenith angle is another critical factor that controls the SW CREs locally. Thus, sampling data from the model to match with the satellite orbit timing and scanning angles require particular care.

Consider that the observation and simulation have exactly the same cloud transmittance for a pair of $\cos\theta_0$ and α_s. However, if their joint frequency of $\cos\theta_0$ and α_s differs, the domain averages from observation and simulation would differ. Indeed, in this study, the joint frequencies are different among them (Figure S1 in the supporting information) due to differences in (1) sampling method and in (2) spatial distribution of α_s (Figure 3). The observed samples are taken over Sun-synchronous orbits and the simulated samples are global snapshots taken every 3 h. To avoid the dependence, we employ the following averaging scheme in calculation of CREs. Define $i = 1, \ldots, n$ bins for $\cos\theta_0$ and $j = 1, \ldots, m$ bins for α_s. The midpoints of both bins range from 0 to 1 with 0.1 width. The domain-averaged, adjusted x for simulation is

$$\langle x\rangle_s^a = \frac{1}{N_{\rm obs}} \sum_{j=1}^{m} \sum_{i=1}^{n} \langle x\rangle_s^{i,j} N_{\rm obs}^{i,j}, \tag{6}$$

where $N_{\rm obs}$ is the total number of observed samples, ${N_{\rm obs}}^{i,j}$ is the number of observed samples for the (i, j) pair of $\cos\theta_0$ and α_s, and $\langle x\rangle_s^{i,j}$ is the mean of the simulated x for the pair. The domain-averaged, adjusted x

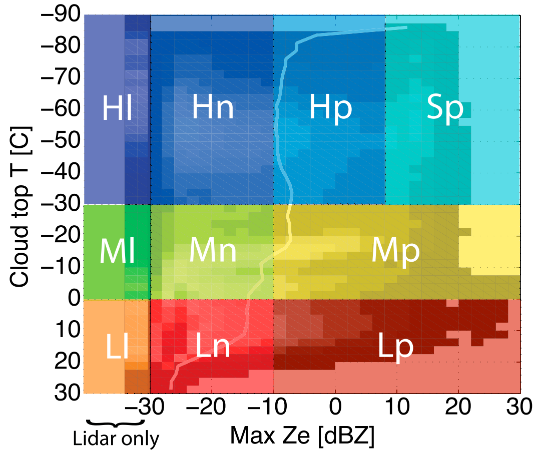

Figure 1. Cloud-type diagram based on Z_{mx} and CTT, obtained globally from CSCA-MD. The first letters "H," "S," "M," and "L" mean high, storm, (potentially) mixed-phase, and liquid clouds. The second letters "l," "n," and "p" denote lidar-only-detected, nonprecipitating, and precipitating clouds. The background shows the joint PDF of the two variables.

for observation is the arithmetic mean calculated with the observed x for the (i, j) pair. For footprint-averaged, adjusted quantities, N_{obs} and $N_{obs}{}^{i,j}$ are obtained only from cloudy samples with use of C4.

In the following comparison of clear-sky and all-sky fluxes, the difference in local time sampled is taken into account by replacing the simulated marginal distribution of $\cos\theta_0$ with the observed one during the averaging procedure.

2.5. Cloud-Type Diagram

This study introduces a simple way to assign a cloud type for each vertical profile of the radar and lidar signals. The approach is similar to the CloudSat Project Level 2 cloud scenario classification product [*Sassen and Wang*, 2008] and combined radar and lidar cloud scenario classification product [*Sassen et al.*, 2008]. The product defines eight cloud types and takes into account horizontal continuity and variability of clouds. Here as an alternative cloud classification, we propose a pair of simple and physically based thresholds to help evaluate the model. The major reason for proposing this simple cloud type is that Sassen and Wang method is a set of sophisticated decision trees with use of MODIS in addition to CloudSat and CALIPSO. This would make it hard to attribute the difference in cloud scenarios between observation and simulation to those in the cloud macrocharacteristics and microcharacteristics. In addition, we feel that a simple categorization is good enough to elucidate the model characteristics, given our ability of simulating cloud systems.

The simple cloud-type diagram categorizes clouds with the cloud top temperature (CTT) and maximum Z_e (Z_{mx}) of a cloud layer (Figure 1). The Z_{mx} is used to relate the layer to the precipitation occurrence and CTT to the phase of hydrometeors (see Appendix A1 for physical interpretation). Cloudy grids in each vertical profile of the signals are specified with the C4 scheme (radar-or-lidar mask). A single cloud layer is defined as a continuous section of cloudy grid boxes, and cloud layers are separated by at least one grid box. Typically, grid boxes near the top of a layer are defined by the lidar signal (C2) and grid boxes below are by the radar signal (C1). CTT is defined as the temperature at the highest grid box of a cloud layer, and the temperature is taken from European Centre for Medium-Range Weather Forecasts (ECMWF) analysis. We assign "lidar-only detection" as the smallest Z_{mx} bin ($-32 < Z_{mx} < -30$ dBZ) for the cloud layers without significant radar signals, as in *Zhang et al.* [2010].

Along the CTT axis, the domain is divided into three groups. The lower threshold of 0°C defines liquid clouds "L." The background gray filling in Figure 1 shows a joint probability density function (PDF) of CTT and Z_{mx} constructed from the global observation of CSCA-MD. As the joint PDF suggests, there is a local minimum of frequency for CTT at −28°C. Therefore, we assign clouds with CTT between 0 and −28°C as (potentially) mixed-phase clouds "M." Clouds with CTT below −28°C are called high clouds "H." The clouds are also defined by their lidar and radar signals, which scale the horizontal axis. Clouds that are detected by radar are divided into two types, for both the mixed-phase and liquid regions, and into three types for high clouds with thresholds of −10 and 8 dBZ. According to the global joint PDF, there is a mode around $Z_{mx} = 13$ at CTT below −40°C. These samples indicate deep precipitating clouds, so we call the category as precipitating storm clouds "Sp."

In the process of applying the cloud type to the simulation data set, characteristics of the radar and lidar are taken into account automatically with Joint Simulator and with cloud mask generation [*Hashino et al.*, 2013].

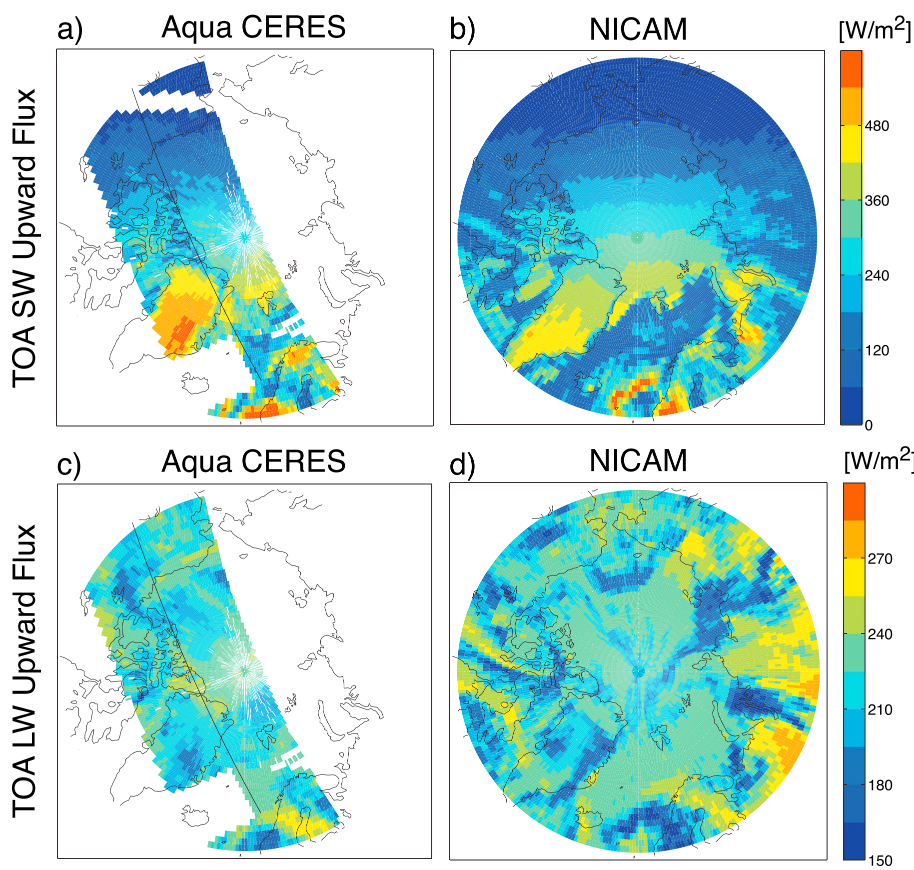

Figure 2. TOA upwelling SW and LW fluxes. (a, c) Observations by Aqua CERES and (b, d) simulations from NICAM/Joint Simulator. Figures 2a and 2b show SW fluxes and Figures 2c and 2d show LW fluxes. The satellite orbit is indicated by the black line in Figure 2c. Both of the observations and simulations were averaged into $1 \times 1°$ grids for display purpose.

Readers are referred to Appendix A for discussion on direct comparison of CTT and Z_{mx} between the observation and simulation and statistical relation between the cloud types and categories of the CloudSat Level 2 cloud scenario.

3. Results

In this section, we characterize the observed and simulated CREs, defined with equations (1)–(4) in section 2.3 , in application of the newly defined cloud type over the Arctic band (65–80°N). Special care is taken for sampling differences between observation and simulation, which can particularly affect the statistics on SW fluxes. It is noted that simulated broadband fluxes shown in this section are calculated with Mie approximation, and uncertainty due to nonspherical ice scattering is discussed in section 4.3.

3.1. Spatial Distribution of Signals

Comparison of the outgoing radiation gives a quick view on model biases in clouds and surface albedo. Observations at 12 Z 19 June show a large TOA SW upward flux (i.e., $F^{\uparrow}_{\mathrm{SW,TOA}}$ exceeds 540 W m^{-2}) over Greenland (Figure 2a), which is underestimated by the simulation (Figure 2b). The outgoing longwave radiation (OLR or $F^{\uparrow}_{\mathrm{LW,TOA}}$) at the same time is shown in Figures 2c and 2d. The low value of the LW flux (below 210 W m^{-2}), in addition to the large SW flux, over Greenland suggests that the area is mostly covered by high clouds associated with a synoptic-scale cloud system. NICAM also underestimates the LW upward flux over Greenland. Thus, as found in Figure 1, NICAM tends to underestimate the cloud top temperature. The underestimated SW upward flux suggests that NICAM also underestimates the cloud optical thickness and/or surface albedo over this region.

Table 2. Footprint-Average, $\cos\theta_0$-Adjusted Clear-Sky Fluxes (W m^{-2}) in the Arctic (65°N–80°N)[a]

17 to 25 June

	TOA UP		SFC DOWN		SFC NET	
	SW	LW	SW	LW	SW	LW
CCCM	158.5 (114.4)	243.8 (17.0)	389.4 (272.2)	263.4 (39.8)	280.1 (224.9)	−68.0 (34.6)
NICAM	181.5 (141.8)	244.2 (12.6)	391.1 (260.3)	258.2 (32.4)	240.7 (202.6)	−77.4 (27.3)
Difference	23.0	0.4	1.7	−5.2	−39.4	−9.3
Aerosol radiative elements	3.4 (5.5)	−0.2 (0.3)	−7.3 (7.6)	0.6 (0.9)	−5.4 (6.2)	0.6 (0.9)

[a]All averages calculated during daytime with a solar zenith angle below 85°. The values enclosed by parentheses are the standard deviation. Difference is defined as NICAM-CCCM.

3.2. Clear-Sky and All-Sky Fluxes

The footprint-averaged, $\cos\theta_0$-adjusted clear-sky fluxes and corresponding standard deviation are listed in Table 2 for the CCCM and NICAM along with the estimates of aerosol radiative elements (*AE*). *AE*s were calculated as the average differences of clean and with aerosol fluxes from CCCM using 1 month data. The clear-sky fluxes (denoted as *F*: flux, ↓: downward, ↑: upward, and no arrow for net) were obtained for 17 to 25 June with use of C4. Comparison of the NICAM-CCCM difference and *AE* indicates that the simulated clear-sky $F^{\downarrow}_{\mathrm{SW,SFC}}$ agrees well with the observation within one standard deviation of the $AE^{\downarrow}_{\mathrm{SW,SFC}}$. On the other hand, the clear-sky $F^{\uparrow}_{\mathrm{SW,TOA}}$ is overestimated by 23.0 W m^{-2} as well as the standard deviation. This is likely related to the bias in surface albedo (Figure 3); the average albedo for NICAM in 65–80°N is 0.36, while the one for CCCM is 0.31. Correspondingly, clear-sky $F_{\mathrm{SW,SFC}}$ is 39 W m^{-2} less than the retrieved one. As for LW fluxes, clear-sky $F^{\uparrow}_{\mathrm{LW,TOA}}$ is well simulated, but the $F^{\downarrow}_{\mathrm{LW,SFC}}$ and $F_{\mathrm{LW,SFC}}$ are smaller than the retrieved fluxes by 5 and 9 W m^{-2}, respectively. Further analysis revealed that these biases are related to smaller *T* below 800 hPa level by about 2 K and larger surface skin temperature by about 3 K compared with the Goddard Earth Observing System (GEOS-5) data used in CCCM.

Table 3 lists the domain-averaged, $\cos\theta_0$-adjusted all-sky fluxes and the standard deviation. Good agreement occurs for the $F^{\uparrow}_{\mathrm{LW,TOA}}$ and $F^{\downarrow}_{\mathrm{LW,SFC}}$, but a large bias of 11 W m^{-2} is found for the $F_{\mathrm{LW,SFC}}$. All-sky $F^{\downarrow}_{\mathrm{SW,SFC}}$ is significantly overestimated by 29 W m^{-2}. The aerosol radiative effect retrieved with CCCM for the $F^{\downarrow}_{\mathrm{SW,SFC}}$ is −9 W m^{-2}, and the remaining 20 W m^{-2} cannot be explained. As mentioned in section 2.2, the retrieved $F^{\downarrow}_{\mathrm{SW,SFC}}$ has biases up to 2 ~ 5 W m^{-2} compared to ground observation, and the uncertainties related to modeled parameters, including aerosol and clouds, are 8 ~ 10 W m^{-2}. Thus, the underestimation of all-sky $F^{\downarrow}_{\mathrm{SW,SFC}}$ and $F_{\mathrm{SW,SFC}}$ is significant, but all-sky $F^{\uparrow}_{\mathrm{SW,TOA}}$ and the LW fluxes are in agreement with CCCM within the uncertainty.

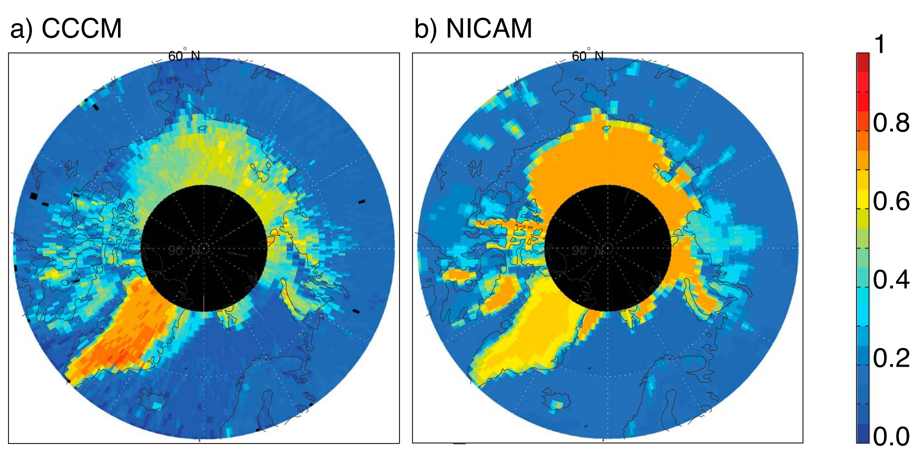

Figure 3. Surface albedo over the Arctic. (a) Calculated from the all-sky upward and downward shortwave fluxes at the surface for CCCM. (b) Same as Figure 3a except for NICAM.

Table 3. Domain-Average, $\cos\theta_0$-Adjusted All-Sky Fluxes (W m^{-2}) in the Arctic (65°N–80°N)[a]

17 to 25 June

	TOA UP		SFC DOWN		SFC NET	
	SW	LW	SW	LW	SW	LW
CCCM	226.3 (136.7)	225.0 (22.1)	301.5 (236.9)	294.0 (40.1)	208.7 (187.1)	−35.4 (35.5)
NICAM	228.9 (151.9)	222.5 (26.6)	330.7 (242.2)	290.9 (40.6)	196.1 (177.4)	−46.7 (35.5)
Difference	2.7	−2.5	29.2	−3.1	−12.7	−11.2
Aerosol radiative effects	4.6 (7.2)	−0.2 (0.4)	−8.7 (10.4)	0.8 (1.2)	−6.4 (8.5)	0.8 (1.2)

[a]All averages calculated during daytime with a solar zenith angle below 85°. The values enclosed by parentheses are the standard deviation.

3.3. Domain-Averaged Cloud Radiative Effects

The domain-averaged, adjusted CREs are listed in Table 4 for 17–25 June period with standard deviation. It is worthy of noting that the standard deviation (or natural variability) is comparable to the average, suggesting the challenge for simulations to reproduce the average. The simulation underestimated cloud albedo effects at TOA and cloud shading effects at SFC as well as greenhouse effects at SFC. A significant overestimate of 22 W m^{-2} occurs in $\mathrm{CRE}^{\downarrow}_{\mathrm{SW,SFC}}$, and correspondingly the simulated $\mathrm{CRE}^{\uparrow}_{\mathrm{SW,TOA}}$ and $\mathrm{CRE}_{\mathrm{SW,SFC}}$ are larger by more than 16 W m^{-2}. Overestimation of the $\mathrm{CRE}^{\uparrow}_{\mathrm{LW,TOA}}$ is consistent with the lower $F^{\uparrow}_{\mathrm{LW,TOA}}$ over clouds (or colder CTT) from NICAM (Figures 2c and 2d).

It turned out that the simulated cloud fraction N with C4 (0.79) agreed well with the observed one (0.74) (Table 5). Thus, the difference is mostly attributed to the difference in cloud types/microphysics, which is discussed in section 3.5.

3.4. Using 8 Day Simulation to Grasp Monthly Characteristics of CREs

In addition to the 8 day statistics, 1 month statistics was calculated from CCCM (Table 4). Notably, the differences in CREs between the two are only a few watts for all the fluxes. Such variability can stem from solar insolation and weather itself. The solar irradiance at TOA decreases by about 6 W m^{-2} from the beginning to 25 of the month, but the average solar irradiance for 17 to 25 is only 1.4 W m^{-2} smaller than the one for the month. The above suggests that 1 month simulation of NICAM would indicate a similar variability compared to the simulation of 17 to 25. Therefore, it is possible to grasp the model monthly bias in CREs with 8 day simulation.

The corresponding statistics for NICAM was calculated with the 8 day simulation by applying the 1 month joint frequency of $\cos\theta_0$ and α_s (Table 4). The changes in the flux differences (NICAM–CCCM) are only up to 2.1 Wm^{-2} from the 8 day to the 1 month data, and the tendency of biases in NICAM does not change. The following discussion uses the 1 month statistics to obtain larger number of samples from CCCM unless noted, and the general conclusion on model bias does not change even when using the 8 day statistics.

Table 4. Domain-Average, Adjusted Cloud Radiative Effects (W m^{-2}) in the Arctic (65°N–80°N)[a]

	TOA UP		SFC DOWN		SFC NET	
	SW	LW	SW	LW	SW	LW
			17 to 25 June			
CCCM	−76.8 (96.2)	18.4 (20.8)	−116.6 (129.1)	40.4 (30.9)	−89.1 (112.6)	39.6 (30.4)
NICAM	−60.5 (89.7)	22.2 (25.4)	−94.4 (130.3)	32.8 (27.9)	−68.6 (102.2)	31.4 (26.8)
Difference	16.3	3.8	22.2	−7.6	20.5	−8.2
			1 to 30 June			
CCCM	−75.5 (95.9)	18.2 (20.2)	−116.1 (129.1)	41.5 (31.1)	−87.7 (112.2)	40.7 (30.6)
NICAM	−57.8 (87.8)	22.1 (25.3)	−91.8 (128.7)	32.7 (27.9)	−65.8 (100.1)	31.3 (26.7)
Difference	17.7	3.9	24.3	−8.8	21.9	−9.5
Aerosol radiative effects	3.7 (6.4)	−0.2 (0.3)	−6.8 (9.0)	0.6 (1.1)	−5.0 (7.4)	0.6 (1.1)
Beam convolution effects	1.2	−0.4	2.4	−1.4	1.4	−1.4

[a]All averages are calculated during daytime with solar zenith angle less than 85°. The values enclosed by parentheses are the standard deviation.

Table 5. Cloud Fractions and Detection Ratios of the Liquid-Containing and Ice-Only Clouds in the Arctic Band[a]

		Total	Hl	Hn	Hp	Sp	Ml	Mn	Mp	Ll	Ln	Lp
		All (Single layer + Multilayer) Clouds										
Cloud fraction	OBS	0.74	0.02	0.12	0.14	0.03	0.14	0.13	0.10	0.04	0.01	0.00
	SIM	0.79	0.06	0.20	0.25	0.07	0.05	0.03	0.07	0.05	0.01	0.01
		Single-Layer Clouds										
Cloud fraction	OBS	0.56	0.02	0.05	0.09	0.03	0.13	0.10	0.09	0.04	0.01	0.00
	SIM	0.52	0.05	0.12	0.13	0.05	0.05	0.02	0.06	0.04	0.01	0.01
Liquid-containing cloud detection ratio	OBS	0.59	0.09	0.09	0.21	0.12	0.86	0.80	0.77	0.76	0.67	0.57
	SIM	0.23	0.00	0.00	0.05	0.02	0.58	0.27	0.36	1.00	0.91	0.99
Ice-only cloud detection ratio	OBS	0.34	0.91	0.66	0.78	0.87	0.13	0.05	0.21	0.23	0.02	0.03
	SIM	0.66	1.00	1.00	0.91	0.83	0.02	0.64	0.20	0.00	0.03	0.00

[a]The detection ratio is defined as the frequency of single-layer clouds (containing information on hydrometeor phase) over all the single-layer clouds. Notice that total of the two detection ratio (0.93 and 0.89 for observation and simulation) may not add up to 1 because some single-layer clouds are not clearly identified as liquid-containing or ice-only types.

3.5. Decomposition of Cloud Radiative Effects Into Cloud Types

The cloud radiative effect (CRE) has contributions from each cloud-type CRE_i:

$$\mathrm{CRE} = \sum_{i=1}^{10} \mathrm{CRE}_i, \tag{7}$$

$$= \sum_{i=1}^{10} N_i \cdot \mathrm{CE}_i, \tag{8}$$

where N_i and CE_i are the cloud fraction and cloud radiative element for cloud type i ($i = 1, \ldots, 10$). For this purpose, we apply the cloud-type scheme from section 2.5 to a whole vertical layer without dividing it into cloud layers. The CTT and Z_{mx} are obtained as the temperature of the highest cloudy grid and maximum Z_e of the entire profile. This way, a multilayer cloud is counted as a single cloud type. For example, a multilayer cloud with an ice-cloud layer above and a liquid-cloud layer below is identified as an H cloud.

Consider the shortwave downward cloud radiative effects at the surface $\left(\mathrm{CRE}^{\downarrow}_{\mathrm{SW,SFC}}\right)$ and the decomposition into N and $\mathrm{CE}^{\downarrow}_{\mathrm{SW,SFC}}$. As shown by the color fill of Figure 4a and Table 5, the observed value N for mixed-phase clouds is largest in the Arctic (37%) and has a significant contribution (14%) from lidar-only-detected cloud (Ml). Contrary to the observation, simulation predicts more high clouds ($N = 58\%$) than midlevel clouds ($N = 15\%$) (Figure 4b). The difference in $\mathrm{CE}^{\downarrow}_{\mathrm{SW,SFC}}$ (Figure 4c) indicates that NICAM overestimates M and H clouds, particularly Mn, suggesting that the modeled M and H clouds are generally too thin optically. The observations show that the Mn contributes the most (20%) of all cloud types to $\mathrm{CRE}^{\downarrow}_{\mathrm{SW,SFC}}$, followed by Ml and Hp (19%) (Figure 4d). The simulations also show that Hp has the largest contribution (34%) to $\mathrm{CRE}^{\downarrow}_{\mathrm{SW,SFC}}$ (Figure 4e). The difference between the simulation and observation (Figure 4f) indicates that the $\mathrm{CRE}^{\downarrow}_{\mathrm{SW,SFC}}$ of (potentially) mixed-phase clouds is 45 W m^{-2} too large, which is then partially compensated by the high clouds that are 20 W m^{-2} too small. Together with the liquid clouds compensation, this leads to an overestimate by 24 W m^{-2}.

The same compensation among cloud types was found for the simulated $CRE^{\downarrow}_{\mathrm{LW,SFC}}$ (Figure S2). The simulated Hp and Sp creates a larger greenhouse effect than observation, opposite the influence from Ml, Mn, and Mp. In total, the overestimate of high clouds (7 W m^{-2}) compensates the underestimate of M clouds (-16 W m^{-2}), resulting in an underestimate of 9 W m^{-2}.

3.6. Dependence of Cloud Radiative Elements on the Particle Phase at Cloud Tops

In this section we use the lidar cloud particle-type retrieval data available from CSCA-MD and investigate the cloud radiative elements (CEs) for liquid-containing and ice-only clouds. As done in *Hashino et al.* [2013], the phase in the simulation is based on the ratio of liquid and ice mass contents; if the liquid mass content in a grid box exceeds 80% of the total mass content, then the grid box is called a "liquid" grid box. Now we can

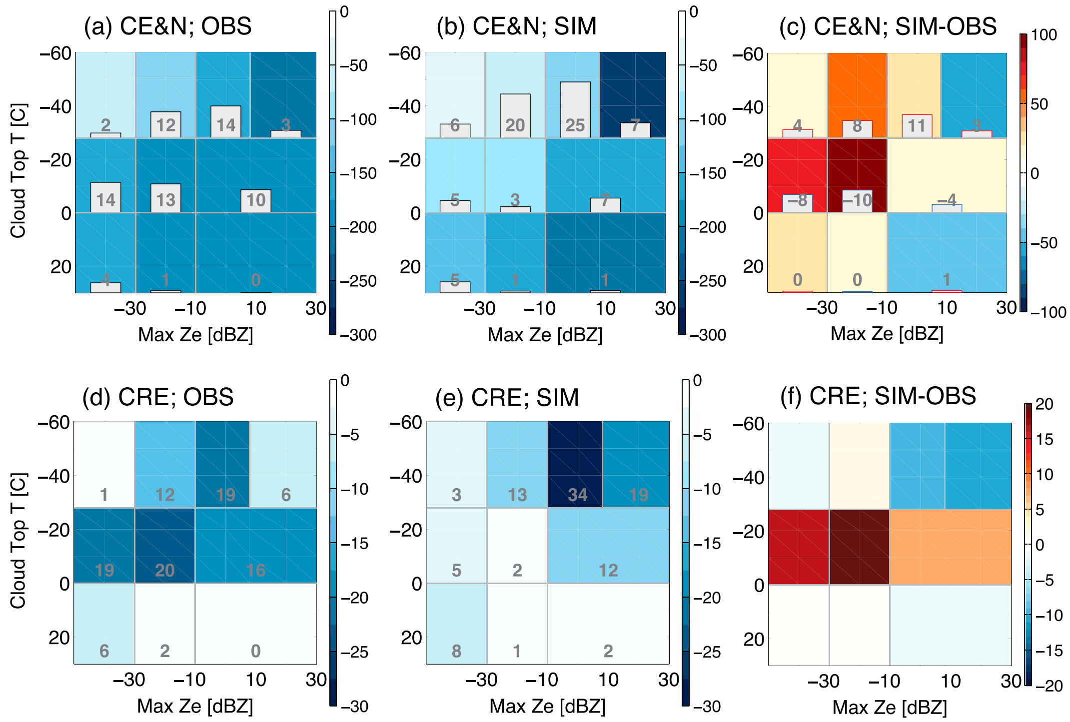

Figure 4. Cloud radiative effects for shortwave surface downward flux, broken up into the 10 cloud types. (a, d) Observation, (b, e) simulation, and (c, f) the difference. Figures 4a–4c show the average cloud radiative elements by color fill and the cloud fraction by the histograms. Figures 4d–4f show the cloud radiative effects of cloud type by color fill and the contribution to the total cloud radiative effects in a percentage.

define cloud layers with at least one liquid grid box in the C2 mask as liquid-containing clouds and define those with all "ice" grid boxes as ice-only clouds.

For the sake of simplicity, only single-layer clouds are studied. As listed in Table 5, the cloud fraction of single-layer clouds (N) is 0.56 in CSCA-MD, indicating that the multilayer clouds account for about 24% of the total N, which agrees well with the annual estimate of *Li et al.* [2011]. The multilayer clouds mostly occur with Hn, Hp, and Mn clouds. NICAM simulates the N for single and multilayer clouds very well.

The high detection of liquid-containing cloud layers characterizes the observed M clouds, which is underestimated by NICAM. The phase retrieval scheme (bottom half of Table 5) shows very high occurrences of liquid-topped Ml (86%), Mn (80%), and Mp (74%), and their occurrence decreases toward larger Z_{mx}. This trend may indicate glaciation of supercooled droplets, followed by aggregation and riming to produce precipitating ice particles, which leads to larger Z_e according to ground-based observations [e.g., *Shupe et al.*, 2008]. More than 8% of H clouds also contain liquid phase particles. Overall, 59% of the single-layer clouds contain liquid hydrometeors in the Arctic band. The simulation also shows the highest detection ratio for Ml for liquid particles (58%), followed by Mp and Mn. However, for all clouds, the simulation generally underestimates the occurrence of liquid hydrometeors and overestimates the occurrence of ice.

Combined use of the CALIPSO cloud particle retrieval and CCCM surface fluxes reveals the strong dependency of observed net shortwave cloud radiative elements at the surface on the particle phase as well as the weakness of the simulation. First of all, magnitudes of the observed $CE_{SW,SFC}$ generally increase with Z_{mx} associated with the cloud types for both the phases (upper half of Table 6), indicating correlation between Z_{mx} and cloud optical thickness (COT). Comparison of the observed $CE_{SW,SFC}$ of liquid-containing and ice-only clouds indicates that the flux difference for M clouds is about 9–42 W m^{-2} (Table 6). Furthermore, a large flux difference due to the phase occurs with Hn (26 W m^{-2}) and Hp (15 W m^{-2}). However, except for Sp clouds, the differences between the simulated liquid-containing and ice-only clouds exceed 60 W m^{-2}. As seen in Figure 4c, the overestimate for ice-only single-layer clouds is reflected in the CE for the case of single plus multiple layers.

Table 6. Observed and Simulated Surface Net Cloud Radiative Elements (W m^{-2}) of Single-Layer Clouds in the Arctic Band[a]

		Hl	Hn	Hp	Sp	Ml	Mn	Mp	Ll	Ln	Lp
					SW						
Liquid-containing clouds	OBS	−24	−74	−117	−174	−118	−146	−139	−143	−200	−244
	SIM			*−168*	*−191*	**−76**	**−116**	*−162*	**−108**	**−137**	**−167**
Ice-only clouds	OBS	−27	−48	−101	−168	−76	−130	−130			
	SIM	**−13**	**−21**	**−60**	−171	**−14**	**−25**	**−45**			
					LW						
Liquid-containing clouds	OBS	12	40	58	56	65	65	64	60	66	66
	SIM			56	54	56	*47*	55	55	*49*	*54*
Ice-only clouds	OBS	10	20	46	53	51	53	57			
	SIM	8	13	*36*	57	*24*	*16*	*33*			

[a]Mean cloud radiative elements calculated for liquid-containing and ice-only clouds using the particle-type retrieval of *Yoshida et al.* [2010]. Simulated CEs that are underestimated (overestimated) from the observation by more than 10 W m^{-2} are italicized (in bold).

For longwave, the observed $CE_{LW,SFC}$ is found to be less sensitive to the phase of hydrometeors than the $CE_{SW,SFC}$ (bottom half of Table 6). The H clouds have a difference up to 19 W m^{-2}, whereas the M clouds have up to 14 W m^{-2}. Agreement between the observed and simulated $CE_{LW,SFC}$ is particularly poor for the ice-only M clouds. As with the SW, the simulated dependence on the phase tends to be larger than observation, reaching 32 W m^{-2} for Ml.

3.7. Cloud Microphysical Diagnosis

In this section we associate the biases in the simulated CE to cloud microphysics by using BETTER (beta-temperature radar-conditioned diagram) analysis. This analysis was introduced by *Hashino et al.* [2013] to determine the mass-equivalent effective radius $R_{\mathrm{eff},m}$ and mass content of hydrometeors. In this method, a set of joint PDFs of the lidar backscattering coefficient β_{532} and air temperature is constructed for a small range of radar reflectivity Z_e. In general, a larger backscattering coefficient β_{532} for a given Z_e range means larger mass content and a smaller $R_{\mathrm{eff},m}$. We constructed the BETTER diagrams for the cloud types introduced above except for the lidar-only-detected cloud layers. In contrast to the *Hashino et al.* [2013] work, which used only cloud top samples, here we analyze samples from all the grid boxes in a cloud layer. In the following, we use Hn and Mn as examples. Because the domain average cloud optical thickness (COT) of these cloud types are 2.59 and 3.41 in the simulation, it is expected that the lidar can penetrate most of the grid boxes in the cloud layers [*Baum et al.,* 2011] and the cloud microphysics inferred with the radar-and-lidar diagnosis is related to the downward broadband fluxes at surface.

Consider the BETTER diagrams of Hn cloud layers. The observation in Figure 5 (left column) has a single dominant mode (yellowish fills) for a given Z_e range and it shifts to warmer temperature with Z_e. As indicated by joint PDFs of the ice only samples (blue contours), the mode matches well with the one of ice samples and contribution of the ice samples is more than 80%. Joint PDF of the liquid samples (red contours) has two modes, one near the mode of ice samples and another at T warmer than −30°C. The former might be related to haze particles in cirrus. The latter is likely related to mixed-phase layers that are connected to upper ice clouds with CTT < -28°C. The control simulation (middle column) shows two modes for all the Z_e ranges that are solely created by ice clouds. As discussed in *Hashino et al.* [2013], the small mode is due to snow-dominant grid boxes, the large mode to cloud ice-dominant grid boxes. It appears that the large mode is fairly close to the observed mode, whereas the small one is situated on the left side of the observed mode. Comparison of the modes suggest two things: (1) For simulated cloud ice-dominant clouds, the ice water content (IWC), and $R_{\mathrm{eff},m}$ are similar to the observation. (2) For simulated snow-dominant clouds, IWC is underestimated and $R_{\mathrm{eff},m}$ is overestimated. Overall, the conditional mean (black dash lines) is underestimated for all Z_e ranges. Correspondingly, the $CE^{\downarrow}_{SW,SFC}$ for Hn is overestimated (Figure 4c). Therefore, the bias of snow (larger size or less IWC) appears to lead to an underestimate of COT and thus the positive bias in the $CE^{\downarrow}_{SW,SFC}$. Also, the underestimate of the $CE^{\downarrow}_{LW,SFC}$ (not shown) is likely related to the snow bias.

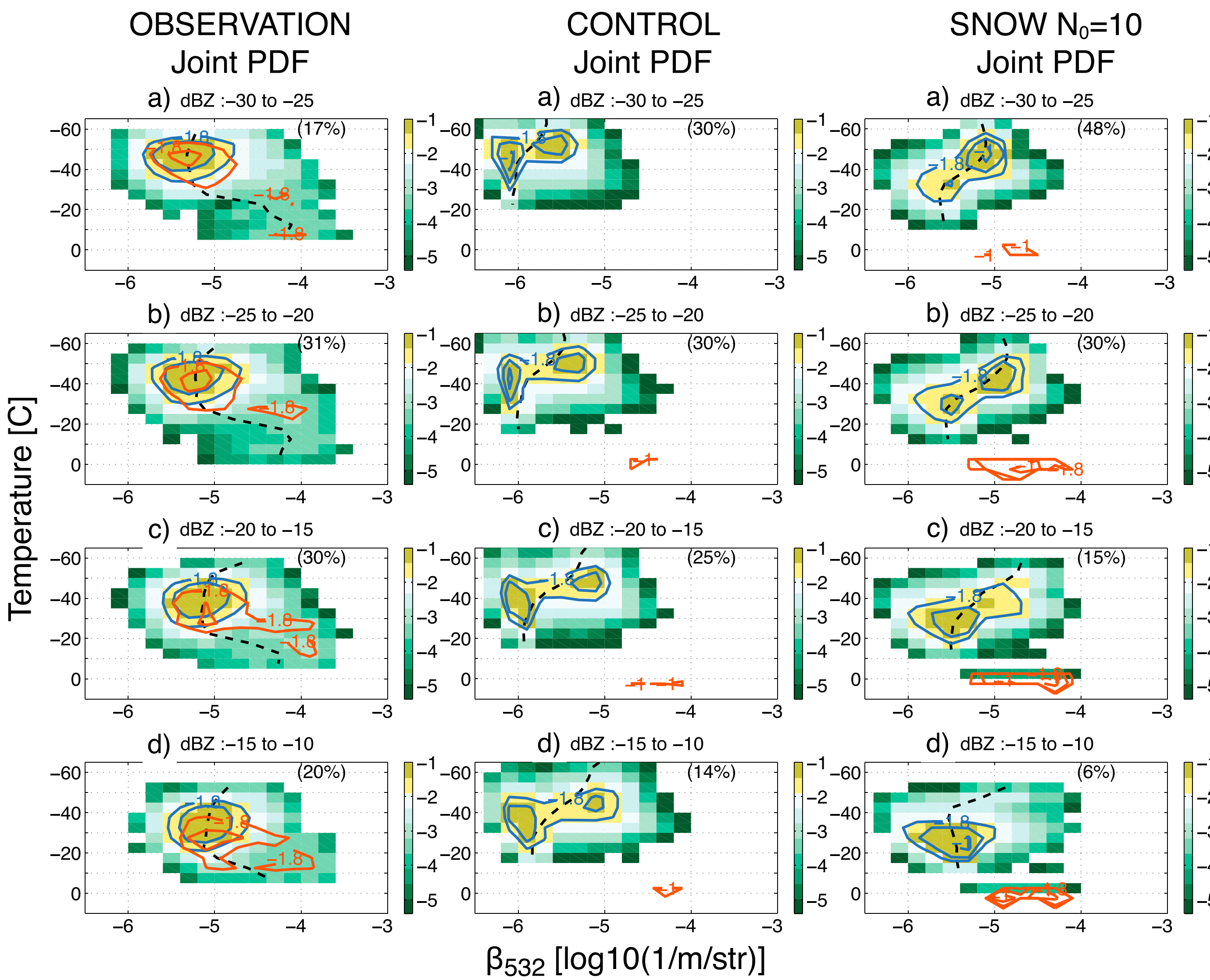

Figure 5. Beta-temperature radar-conditioned (BETTER) diagram for (left column) observation, (middle column) control, and (right column) SN10 for Hn cloud layers in the Arctic. The color fill indicates the joint PDF of all samples with a logarithmic scale, which is segregated from −5.4 to −1.0 by 0.4. The blue and red contours are the joint PDF of ice and liquid samples, respectively, which are given at −1.8, −1.4, and −1.0. The black dash lines are the mean conditioned on temperature. The percentage in parentheses indicates the fraction of the dBZ range within samples that belong to the Hn cloud type.

Now consider the BETTER diagrams for Mn cloud layers. The observation (Figure 6, left column) possesses a dominant mode (yellowish fills) for Z_e below −15 dBZ. Joint PDF of the liquid samples (red contours) is collocated with the mode and they contribute to it more than 80%. Note that the ice clouds (blue contours) have a mode between −5 and −4 on the left of the liquid mode. This coupling probably indicates freezing of liquid particles and subsequent growth of ice particles in mixed-phase single layer clouds. As Z_e range increases, another mode of the ice clouds emerges at β_{532} below −4.5. It is probably unrelated to the mixed-phase clouds at T warmer than −20°C. Interestingly, for the largest Z_e range (d), the mode with β_{532} ~ −5 and T between −10 and −15°C is equally contributed by liquid and ice clouds. The control simulation (Figure 6, middle column) indicates two modes, which are clearly separated to ice and liquid clouds. The fact that the coupling of ice and liquid seen for observation is absent suggests freezing process is not simulated well. The β_{532} of the ice mode is around −6, which suggests a smaller IWC and larger $R_{\mathrm{eff},m}$ than the observation. Similarly, the liquid mode of smaller β_{532} suggests a smaller LWC and larger R_{eff}, and in addition the mode is situated in warmer T than the observation. Observations show that supercooled liquid clouds have a COT

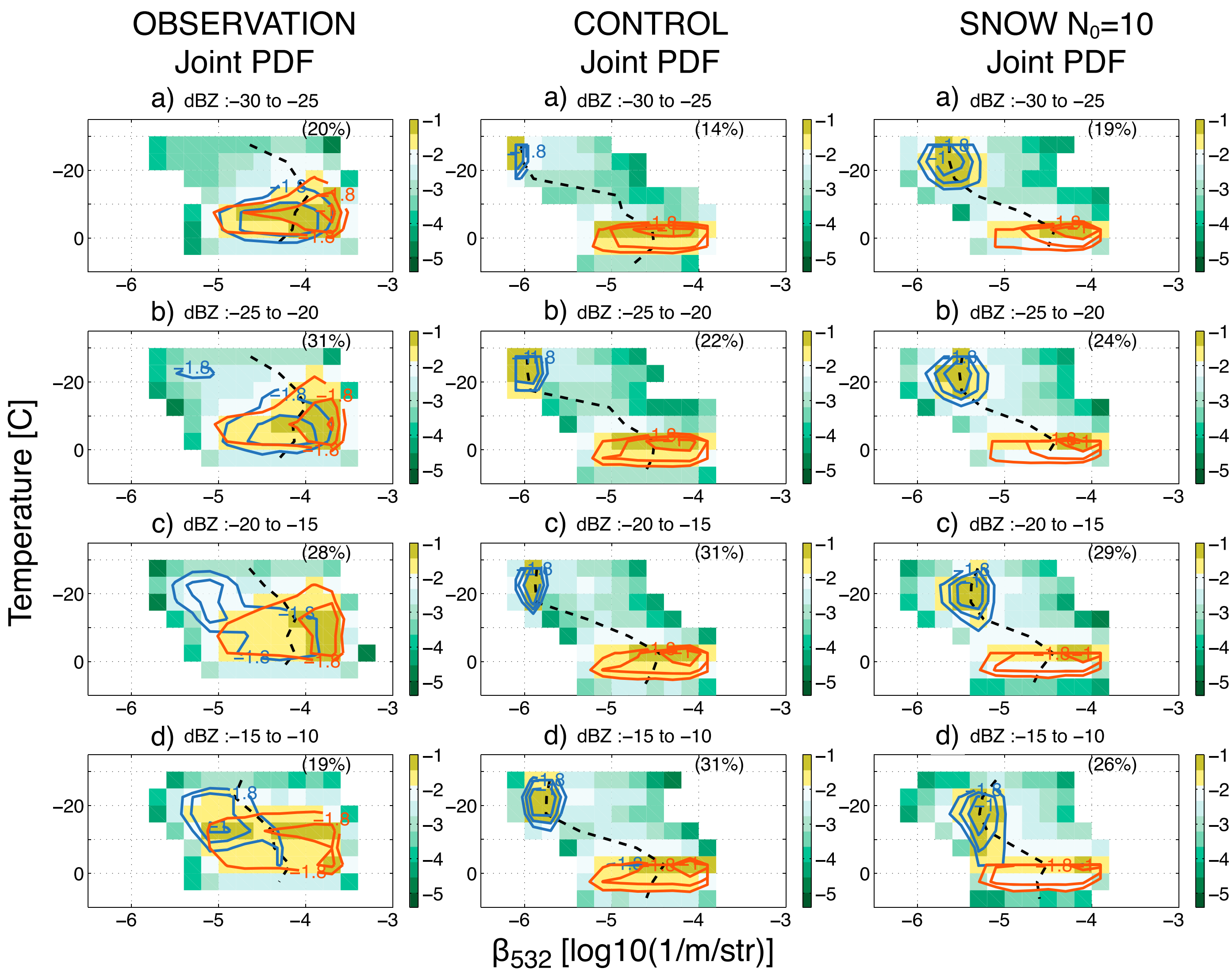

Figure 6. Same as Figure 5 except for Mn cloud layers.

large enough to produce a CE exceeding that of ice-only clouds [e.g., *Shupe and Intrieri,* 2004]. Therefore, the overestimate of $CE^{\downarrow}_{SW,SFC}$ seen in Figure 4c for Mn clouds can be attributed to the lack of the liquid clouds in cold temperatures ($T < -10$°C) as well as the smaller β_{532} itself.

4. Discussion

In this section, we study the sensitivity of CREs to the parameters used in the forward simulation, namely, those assumed for cloud microphysics, surface albedo, and single-scattering parameters. The goals are to support the above conclusions on the simulated cloud microphysics and to seek a way to improve the biases. In the process, the parameters are changed only in simulating the signals—we did not rerun NICAM with those parameters. For the sensitivity tests, we simulated the signals for only 19 June, from 00 Z to 21 Z (Control-19, Table 7) because the solar insolation at TOA is similar to the one for the 8 day samples. To reduce computational burden, the number of sampled vertical columns was reduced by 1/4 in each horizontal direction and beam convolution was not implemented on the broadband signals. The beam convolution effects (BEs) were calculated as the average differences of fluxes calculated with and without beam convolution scheme applied to the NICAM data set. The BEs bring minor (about 2 W m^{-2}) differences in the CREs (bottom of Table 4), which supports the setting of forward calculation.

Table 7. Domain-Average-Adjusted Cloud Radiative Effects (W m^{-2}) in the Arctic (65°N–80°N)[a]

	TOA UP		SFC DOWN		SFC NET		
	SW	LW	SW	LW	SW	LW	COT
Control-19	−55.1	21.7	−89.3	34.6	−62.8	33.1	9.42
CI20	−59.7	26.6	−93.6	35.1	−65.8	33.6	10.07
SN0.1	−54.9	22.6	−90.1	34.8	−63.4	33.3	9.52
SN10	−60.3	28.4	−101.2	37.6	−71.4	36.0	10.05
CW1.5	−67.6	22.1	−98.9	35.2	−76.5	33.7	11.24
AMOD	−64.2	24.3	−95.0	37.2	−72.5	36.6	9.50

[a]COT is the average cloud optical thickness calculated in a visible band between 0.435 and 0.678 μm.

4.1. Sensitivity of CREs to Cloud Microphysical Parameters

Seven sensitivity tests were considered by varying microphysical parameters, following *Hashino et al.* [2013], and the improvement relative to Control-19 is discussed. Note that Mie solution for spheres is applied to the sensitivity tests discussed in this section. To investigate the importance of cloud ice, we reduced R_{eff} for ice particles in the simulated signals from 40 to 20 μm. This change increases the optical thickness of ice clouds, decreasing $CE^{\downarrow}_{SW,SFC}$ for most cloud types by up to 11 W m^{-2}, and thus improving agreement (Figure 7b). The SW CRE decreased by about 3 to 5 W m^{-2} and average cloud optical thickness (COT) in the domain increased from 9.42 to 10.07 (CI20, Table 7), compared to Control-19. At the same time, it increases the greenhouse effect at TOA but does not affect the SFC LW fluxes very much because the "cloud ice" category is usually situated at cloud top.

The snow category of NSW6 has a large impact on the broadband fluxes [*Hashino et al.* [2013]]. In NSW6, this category uses a particle size distribution

$$N(D) = N_0 \ \exp(-\lambda D), \quad (9)$$

where $N(D)$ is the number concentration per size, N_0 is the intercept parameter, λ is the slope parameter, and D is the maximum dimension. At a fixed IWC, when N_0 increases, λ increases and the resulting R_{eff} decreases. Values of $N_0 = 0.1$ and 10 cm^{-4} result in smaller R_{eff} as compared to that with $N_0 = 0.03$ cm^{-4} (Control). The C

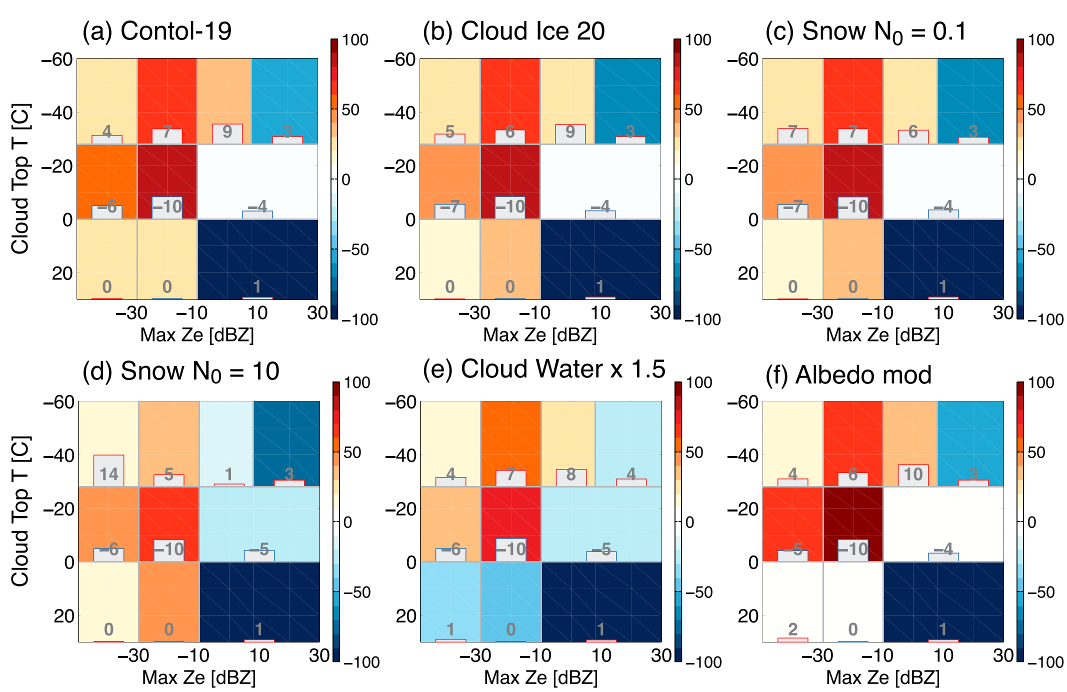

Figure 7. Biases in average cloud radiative element for shortwave surface downward flux (color fills) and cloud fractions (histogram and number). Each panel corresponds to the sensitivity experiment listed in Table 4.

$E^{\downarrow}_{SW,SFC}$ bias in high clouds with $N_0 = 0.1\ cm^{-4}$ is slightly improved (Figure 7c), similar to CI20, but the $CRE^{\downarrow}_{SW,SFC}$ was not improved (SN0.1, Table 7) as much as CI20 due to reduced N for Hp. When N_0 is increased 100-fold, significant improvements occur for H and M cloud types (Figure 7d); in particular, the CE of Hp clouds decreases by 56 W m^{-2}, becoming negatively biased. The N value of Hl now increases by 10% due to the decrease in R_{eff} for the other H-type clouds. The smaller snow R_{eff} increased COT to 10.05 and significantly reduced the values of SW CRE (SN10, Table 7). In contrast to its impact on cloud ice, this modification has positive impacts on the $CRE_{LW,SFC}$ and $CRE^{\downarrow}_{LW,SFC}$ because snow typically extends into the lower levels with larger depth than cloud ice and contributes more to the cloud microphysics of cloud bases.

Among the above cases, the cloud water content has the largest impact on the SW CREs by changing the optical thickness of M and L clouds. When we increase the water content of the cloud water category 1.5-fold, all SW CREs (COT) increase by about 10 W m^{-2} (1.8) compared to Control-19, while having little effect on the LW CREs (CW1.5, Table 7). The small effect on the LW CREs is due to the low cloud top height. The $CE^{\downarrow}_{SW,SFC}$ of M and L clouds were decreased as much as 22 and 71 W m^{-2}, respectively. As a result, the positive bias for high clouds, Ml, and Mn were reduced, while those for L clouds became even more negatively biased (Figure 7e).

Modification of the surface albedo in the NICAM is not enough to improve the biases in SW CREs and CEs. As discussed above, the surface albedo used in the Control simulation is quite different from the one of CCCM (Figure 3). By setting the CCCM surface albedo and emissivity, the domain-averaged, adjusted SW CREs become about 6 ~ 10 W m^{-2} closer to observation (AMOD, Table 7). This change is solely due to the changes in cloud types that are classified into each bin of surface albedo in equation (6). The overall biases in $CE^{\downarrow}_{SW,SFC}$ (Figure 7f) remain qualitatively similar to Control-19, although the magnitudes of bias decrease by about 13 and 20 W m^{-2} for Ln and Lp. These cases underscore the importance of improving cloud microphysical properties and cloud fractions because fixing the surface albedo may lead to only about 10 W m^{-2} decrease in the domain-averaged, adjusted SW CREs.

4.2. Connecting Biases in Cloud Radiative Element and Cloud Microphysics

The changes in CEs due to the changes in the microphysics parameters can be identified using the BETTER diagram, particularly for optically thin clouds. In the case of SN10, the bias of Hn cloud layers was reduced by 38 W m^{-2} for Hn cloud layers, compared to Control-19 (Figure 7d). According to the BETTER diagram for SN10 Hn (Figure 5, right column), use of large N_0 (=10 cm^{-4}) brings the two modes (dark yellow) closer and shifts them to larger values. However, the modes of β_{532} are still underestimated for Z_e above −20 dBZ, which imply a larger $R_{eff,m}$ for the ranges. We infer that this results in the remaining underestimate of cloud albedo effects for Hn by 32 W m^{-2}. As for Mn clouds, SN10 reduces the positive bias in the $CE^{\downarrow}_{SW,SFC}$ (Figure 7d). Similar to the case of Hn clouds, the mean β_{532} increase from control for all the Z_e ranges (Figure 6, right column). This is a consequence of the reduced $R_{eff,m}$ for the snow category and a good agreement with observation can be identified in terms of ice clouds (compare blue contours). Still, the overestimate by 66 W m^{-2} remains in the $CE^{\downarrow}_{SW,SFC}$ (Figure 7d), and further improvement could be obtained by increasing β_{532} associated with liquid samples.

For optically thick precipitating clouds, the biases in the $CE^{\downarrow}_{SW,SFC}$ were not clearly related to the cloud microphysical biases that the BETTER diagram indicates. For instance, the $CE^{\downarrow}_{SW,SFC}$ of Sp was overestimated (Figure 7a), but underestimation of the mean β_{532} was also found for all the Z_e ranges (Figure S3). SN10 showed the increased mean β_{532} in a way similar to Hn, which is still consistent with even larger underestimation in the $CE^{\downarrow}_{SW,SFC}$.

4.3. Sensitivity of CREs on Nonspherical Single Scattering Parameters

As indicated in Table 4, the magnitudes of $CRE^{\uparrow}_{SW,TOA}$ and $CRE^{\downarrow}_{SW,SFC}$ are underestimated with NICAM, but this could be due to single scattering assumption using a Mie solution to some extent. Thus, we quantify the bias due to the single-scattering parameters associated with the spherical assumption. Eight ice crystal habits with severely roughened surface were chosen from *Yang et al.* [2013] database: plate (Plate), solid column (Solid-Col), hollow column (Hol-Col), solid bullet rosette (Solid-BR), hollow bullet rosette (Hol-BR),

Table 8. Impact of Nonspherical Scattering on Domain-Average-Adjusted Cloud Radiative Effects (W m^{-2}) in the Arctic (65°N–80°N)[a]

	TOA UP		SFC DOWN		SFC NET		
	SW	LW	SW	LW	SW	LW	COT
Control-19	−55.1	21.7	−89.3	34.6	−62.8	33.1	9.42
Plate	−57.0	20.4	−92.5	34.3	−65.0	32.9	10.04
Solid-Col	−58.4	17.8	−93.3	33.0	−65.6	31.6	9.42
Hol-Col	−58.8	18.2	−93.8	33.2	−66.0	31.8	9.54
Solid-BR	−63.1	21.3	−98.3	34.2	−69.1	32.8	9.94
Hol-BR	−63.7	22.0	−99.0	34.5	−69.6	33.1	10.19
Plate-5	−61.0	20.3	−95.9	33.7	−67.4	32.3	9.71
Plate-10	−63.3	23.0	−98.3	34.7	−69.1	33.3	10.26
Col-8	−63.5	19.9	−98.5	33.5	−69.2	32.1	9.62
Uncertainty	8.6 (6.7)	5.2 (5.2)	9.7 (6.5)	1.7 (1.7)	6.8 (4.6)	1.7 (1.7)	0.84 (0.84)

[a]Uncertainty is defined as difference of maximum and minimum values among all the cases. The values in parentheses are the difference among only the eight nonspherical particles.

aggregate of five plates (Plate-5), aggregate of 10 plates (Plate-10), and aggregate of eight columns (Col-8). The domain-averaged, adjusted CREs were calculated for 19 June with the database.

Use of the nonspherical single-scattering parameters showed larger magnitudes of SW CREs than those with Mie calculation (Table 8). The largest magnitude in the SW CREs was obtained with Hol-BR, while the smallest with Plate. The habits of polycrystals or multiple components tend to exhibit larger magnitude of SW CREs than the simple crystals like Plate and Solid-Col. It can be mostly attributed to the magnitude of extinction coefficient or COT (Table 8), but for Plate the largest asymmetry parameter led to the smallest SW CREs. The uncertainty of SW CREs, defined as a difference between maximum and minimum values, associated with these different shapes of ice habit is as large as 8.6 (9.7) W m^{-2} for $CRE^{\uparrow}_{SW,TOA}\left(CRE^{\downarrow}_{SW,SFC}\right)$. However, these uncertainties appear to be still smaller than the positive biases in Table 4. Therefore, we conclude that the underestimation of cloud shading effect is robust in NICAM.

The Mie calculation (sphere assumption) of Control-19 for LW was not necessarily the min/max of all the cases (Table 8). Among the LW CREs, the $CRE^{\uparrow}_{LW,TOA}$ shows the largest variability among the different options of ice habit, up to 5.2 W m^{-2}. This is larger than the difference between NICAM and CCCM. On the other hand, the underestimation biases in $CRE^{\downarrow}_{LW,SFC}$ and $CRE_{LW,SFC}$ are significant in NICAM, because of smaller sensitivity to the different options of ice habit. The Solid-Col (Plate-10) tends to have the largest (smallest) extinction at effective radius larger than 10 μm in LW, which results in the largest (smallest) $CRE^{\uparrow}_{LW,TOA}$.

The SW cloud radiative elements for precipitating high clouds are particularly sensitive to the nonspherical ice scattering. For instance, the spread of the flux in Hp $CE^{\downarrow}_{SW,SFC}$ is 16.6 W m^{-2} among the eight habits and the minimum difference from Control-19 is −23.2 W m^{-2} (Figure 8a). However, the diagnosis of NICAM overestimating Hp $CE^{\downarrow}_{SW,SFC}$ is still qualitatively valid since the bias itself is +37.0 W m^{-2} for Hp (Figure 7). The uncertainty (spread due to the different scattering models) in $CE^{\uparrow}_{LW,TOA}$ of Hn, Hp, and Sp is 9.0, 12.1, and 8.9 W m^{-2}. Especially, the difference from Control-19 for Hp varies from −9.3 to +2.8 W m^{-2} (Figure 8b). Since the simulated $CE^{\uparrow}_{LW,TOA}$ for Hn, Hp, and Sp is biased by −9.4, +9.0, and +12.9 W m^{-2}, only Hp changes the sign in bias due to the nonspherical ice models. The uncertainty in LW CEs for M clouds are up to 1.6 W m^{-2} (Figure 8b), which does not alter the diagnosis on M clouds that underestimates all the LW CEs (not shown here). The aforementioned habit dependence of CREs also appears in CEs as indicated by symbols in Figure 8.

5. Summary and Outlook

The cloud radiative effects (CREs) simulated by NICAM with a single-moment cloud microphysics parameterization were evaluated against the collocated A-train observations and retrievals (CSCA-MD including the CCCM data set), i.e., CPR reflectivity, CALIOP 532 nm backscatter, four cloud masks, a cloud particle type

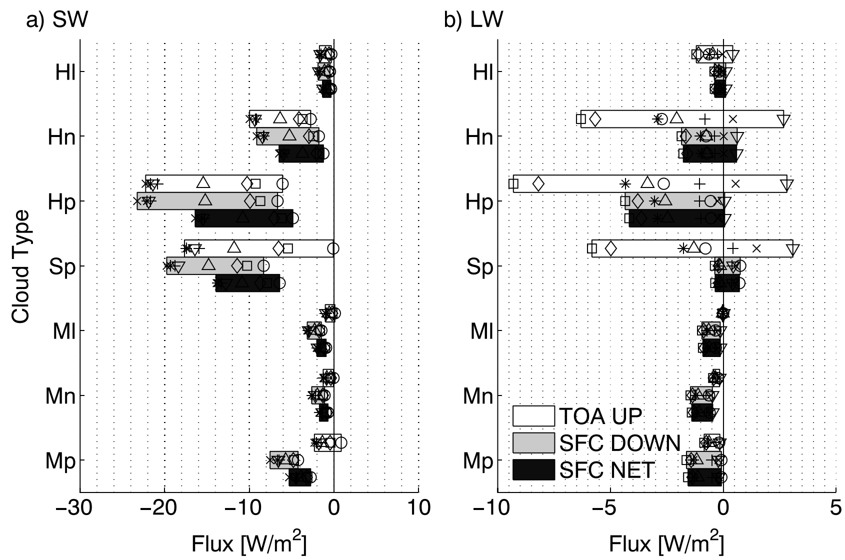

Figure 8. Impact of the nonspherical single-scattering parameters on simulated cloud radiative elements in (a) SW and (b) LW. The fluxes simulated by eight ice habits are plotted relative to Control-19 with the symbols; circles: Plate, squares: Solid-Col, diamonds: Hol-Col, plus signs: Solid-BR, crosses: Hol-BR, upward pointing triangles: Plate-5, downward pointing triangles: Plate-10, and asterisks: Col-8. The solid bars indicate ranges calculated with the seven ice crystal habits, relative to Mie approximation. The vertical axis shows the seven cloud types containing ice particles.

retrieval, and broadband fluxes at TOA and surface. The comparison was mainly conducted in the radiance-backscatter space by simulating the signals from the NICAM outputs with Joint Simulator. The simulation spans from 17 to 25 June 2008, which was evaluated against the observation of the 8 day period and whole month of June. It is concluded that the 8 day period simulation can be still used to obtain the model characteristics for the month.

In this paper, a simple cloud-type scheme was proposed for the purpose of model evaluation. The scheme defines 10 cloud types with the maximum radar reflectivity (including lidar-only detection) and the cloud top temperature (CTT) of cloud layers, and the occurrence of precipitating hydrometeors and the phase of hydrometeors can be associated with the cloud types (see Appendix A for details). The proposed cloud types generally show one-to-one correspondence with the CloudSat Project Level 2 cloud scenario product, although the mixed-phase cloud types were somewhat ambiguous. Comparison of the joint PDF of the maximum radar reflectivity and CTT between simulation and observation itself is useful to characterize the biases and errors in the simulation. NICAM generally overestimated the occurrences of high clouds globally and the occurrences of precipitation in clouds with top temperature above -10°C. But it did not reproduce a distinct precipitating mode with CTT ~ -15°C in the Arctic band.

The SW cloud albedo/shading effects and LW greenhouse effects in the domain were underestimated with the simulation. Since the cloud fractions of single-layer and multilayer clouds were well simulated, the biases boil down to the simulated cloud type and cloud microphysics. Using the above cloud-type scheme, CREs were decomposed into cloud fraction (*N*) and footprint-level cloud radiative effects, termed cloud radiative element (CE). We applied an adjusted domain-averaging based on observed occurrences of surface albedo and solar zenith angle to bypass the differences in those variables between simulation and observation. The major findings are the following:

1. NICAM overestimated the downward SW CRE at the surface by 24 W m^{-2}, and this was mainly due to the model overestimating the CRE for mixed-phase clouds. NICAM overestimated the high-cloud *N*, and this compensated for the overestimated CE and underestimated *N* of the mixed-phase clouds. Similarly, the downward LW CRE at surface was underestimated by 9 W m^{-2} due to too infrequent, too optically thin mixed-phase clouds, yet was partially compensated by too frequent, too optically thin high clouds.
2. Use of the cloud particle-type retrieval improves our understanding of the CE dependence on the particle phase as well as the phase-partitioning problem in the model. The observed liquid-containing single-layer clouds occurred twice as often as the ice-only clouds, whereas NICAM predicted their occurrence as only

one third that of ice-only clouds. The observed SW (LW) net CE shows 9 ~ 42 (6 ~ 14) W m^{-2} differences between the liquid-containing and ice-only mixed-phase clouds. NICAM estimated larger dependency up to 117 (32) W m^{-2} for the SW (LW) fluxes.

3. Using the cloud-type scheme and BETTER diagram, we were able to connect the cloud microphysics and CE of optically thin cloud types. The biases in CE of the nonprecipitating mixed-phase clouds were associated with an underestimate of water content and overestimate of mass-equivalent effective radius for cloud water and snow. We also found an underestimate of the occurrence of supercooled water relative to ice. Coupling of the modes between observed liquid and ice samples suggests active freezing process, which was absent in the simulation.

The above biases in CREs were pronounced in the biases in all-sky fluxes; NICAM overestimated the all-sky SW downward flux at the surface. On the other hand, the all-sky SW upward flux at TOA and all the all-sky LW fluxes agreed with CCCM within the uncertainty. The agreement for the SW upward flux is likely due to the large surface albedo used in NICAM, compared with the one in CCCM. Indeed, NICAM overestimated the clear-sky SW upward flux at TOA by 23 W m^{-2}, which compensated the underestimated cloud albedo at TOA. According to CCCM retrieval, the SW downward fluxes at the surface were reduced by aerosol as much as 9, 7, and 7 W m^{-2} for all-sky, clear-sky, and cloudy sky samples, respectively. Therefore, it is critical to include the aerosol effects in the broadband calculation even when the aerosol particles are explicitly not predicted.

Sensitivity tests in the forward simulation further supported the above diagnosis and suggest a way to improve the CREs. In the offline radiative transfer calculation, the improvement in surface albedo distribution only adds about 5 ~ 10 W m^{-2} to the domain average SW CREs, indicating a need to improve the cloud microphysics. The signals in the BETTER diagram improved when either the mass-equivalent effective radius of snow decreased or the cloud water content increased. Correspondingly, reduction of bias in SW downward surface CE was found for nonprecipitating clouds. However, the biases in the CE of optically thick precipitating clouds were not clearly related to the biases seen in the BETTER diagram. This is because the lidar cannot penetrate the whole cloud layer of such clouds. For these cases, passive microwave observations are expected to be useful to constrain column-integrated quantities like water path, which is a topic of future research.

Uncertainties in CREs and CEs associated with the single-scattering parameters of nonspherical ice particles were investigated to ensure robustness of the diagnoses. The spread of calculated SW (LW) CREs was shown to be as large as about 10 (5) W m^{-2}, and the SW downward CE for high precipitating clouds can be smaller than the control case by 23 W m^{-2}. Even after considering the uncertainties in broadband calculation, the underestimation of SW cloud shading effects and LW downward/net CREs was robust for the NICAM data set used in this study. It is emphasized that the magnitudes of SW CREs and CEs were greater than those calculated with Mie approximation. Efforts should be made toward use of the nonspherical ice models in online broadband calculation of NICAM as well as GCMs.

Previously, a 14 km mesh NICAM simulation with the same cloud microphysical scheme (NSW6) was evaluated by *Kodama et al.* [2012] over 3 months of integration, which indicated a similar bias in cloud fraction and the CREs at TOA over the Arctic. They implemented sensitivity experiments in which the threshold for ice crystals to form snow is changed and fall speed of cloud ice is set finite. As a result, the global SW (LW) CREs at TOA varied by 14 W m^{-2} (67 W m^{-2}), which encompasses the observed CREs. However, none of them was able to match both the SW and LW CREs and to reduce the upper level cloud fraction at the same time. This clearly shows a challenge in tuning the cloud microphysics parameters. It is hoped that the testing of cloud microphysics parameterization with coarse resolutions or stretched grid is effective to reduce the biases in high-resolution runs.

Finally, it is important to recognize that there are large uncertainties in the downward and net fluxes at surface from the CCCM because they involve modeling of aerosol and clouds in addition to thermodynamical states. The small contrast between ice-only clouds and liquid-containing clouds in the retrieved SW and LW CE, compared to the simulated ones, might reflect a deficiency of the retrievals involved, inconsistency between the phase specified in CCCM and the one retrieved with our cloud particle type scheme, and/or larger spatial inhomogeneity in phase for observed clouds. It is important to continue the efforts to reduce the uncertainties for more trustworthy evaluation of numerical weather prediction models and GCMs.

Appendix A: Cloud-Type Diagram

A1. Interpretation of Cloud Top Temperature and Maximum Radar Reflectivity

The 2-D space defined with $Z_{\rm mx}$ and CTT can be associated with existence of precipitating hydrometeors and the phase of hydrometeors as follows. CTT is directly related to the TOA LW upward fluxes for optically thick clouds, and its value helps determine the phase of hydrometeors in a cloud layer. The clouds with CTT above 0°C are assigned as liquid clouds. As homogeneous freezing of cloud droplets typically occurs only below −38°C, CTT values below −38°C generally indicate ice clouds. Those with CTT between 0 and −38°C can be supercooled liquid clouds, ice-only clouds, and mixed-phase clouds [e.g., *Yoshida et al.,* 2010].

Using a $Z_{\rm mx}$ threshold in the cloud type diagram, precipitating and nonprecipitating clouds are separated. This helps us make connection to cloud microphysical parameterization such as autoconversion and accretion of liquid hydrometeors. Unattenuated Z_e exceeding −15 dBZ is usually associated with both liquid and ice precipitating particles in retrieval algorithms such as the CloudSat Project Level 2-C precipitation column algorithm (Table 2) [*Haynes et al.*, 2009]. According to *Wang and Geerts* [2003], the drizzle occurrence increases rapidly from −20 to 10 dBZ in marine stratus clouds, with −15 dBZ considered to be the drizzle threshold. *Stephens and Wood* [2007] use −10 dBZ for defining the precipitating clouds in Tropics. As for solid precipitation, the Z_e-S relationship obtained by *Liu* [2008] shows that −14.4 dBZ indicates 0.01 mm h^{-1} of snowfall. Taken all together, we will consider −10 dBZ of attenuated Z_e as the threshold for precipitating hydrometeors. Finally, since $Z_{\rm mx}$ is generally correlated with microwave optical depth and water path of condensates, the cloud radiative effects are also related to $Z_{\rm mx}$.

It is noted that the lidar is an ideal instrument to identify cloud tops for the sensitivity to small particles and that the cloud radar can detect nonprecipitating and precipitating volumes below the cloud tops. The lidar-only detected clouds correspond to thin clouds with optical thickness as low as 0.01 [*McGill et al.,* 2007] that the radar cannot detect. Also, the lidar detects boundary layer clouds within 1 km of the surface that cannot be seen by the radar due to the surface backscattering. On the other hand, the lidar signals are totally attenuated for clouds with optical thickness greater than 3 [*Baum et al.,* 2011]. Therefore, in case of multilayer clouds the radar likely determines the CTT of lower clouds below optically thick clouds.

A2. Direct Comparison of $Z_{\rm mx}$ and CTT

The characteristic variables Z_{mx} and CTT help provide a physical understanding of the observed and simulated cloud characteristics. In the following, the joint PDFs of Z_{mx} and CTT for the Arctic band (65–82°N) are compared between the observation and simulation (Figure A1). Note that the samples detected only by lidar without Z_{mx} values were included in calculating the PDFs and shown to the left of −30 dBZ. The observed joint PDF in the Arctic shows five modes (Figure A1a). There are two modes with CTT below −35°C, one with Z_{mx} around −24 dBZ and one near 2 dBZ. These likely correspond to nonprecipitating cirrus clouds and deep convective/nimbostratus clouds (Appendix A). Also, for lidar-only detected clouds, CTT has a large value between −10 and 0°C. Note that the occurrence of lidar-only detected clouds is actually 10 times larger than the value shown in the figure. The two modes with CTT above −20°C are nonprecipitating and precipitating clouds. According to the lidar retrieval study of *Yoshida et al.* [2010], for the Arctic band, the occurrence of liquid between −20 and −10°C is about 30%, whereas that between −10 and 0°C is 50 to 75%. Therefore, the three modes above −20°C are likely from supercooled liquid clouds. The mode at CTT ~ −15°C has a significantly larger $Z_{\rm mx}$ than that at CTT > −10°C. It is probably because these clouds include the temperature range (−14 to −17°C) where the vapor deposition growth rate of ice particles reaches a maximum [*Takahashi et al.,* 1991] and where aggregation process is active due to large collision cross-section area of dendritic crystals [*Hashino and Tripoli*, 2011]. This mode indicates precipitation.

In the simulation (Figure A1b) cirrus and deep convective/nimbostratus clouds dominate. This result contrasts with observation in which the low and middle clouds dominate. Also, the mode detected only by lidar and two radar-detected modes for CTT above −30°C occur at warmer temperatures than those of observation. Because CTT is more directly related to the TOA IR-window flux, this implies an overestimate of the TOA upward LW fluxes of the middle and low clouds. Assuming the phase of the particles is the same for simulation and observation, an overestimate of $Z_{\rm mx}$ in the precipitating mode indicates that the simulated

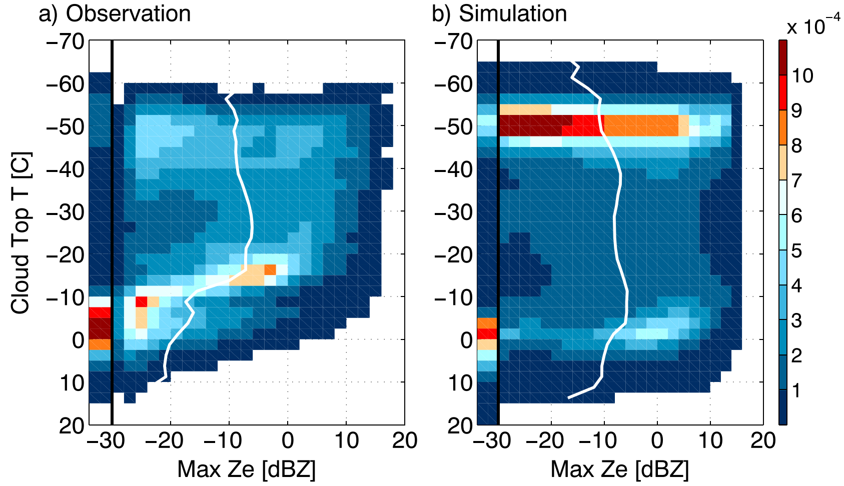

Figure A1. Joint PDFs of CTT (cloud top temperature) and Z_{mx} (maximum radar reflectivity) of cloud layers for Arctic (65–82°N). (a) CSCA-MD and (b) NICAM simulation. The white curves denote the mean conditional of CTT. The samples of cloud layers detected only by lidar without Z_{mx} values were included into the leftmost bins ($-32 < Z_{mx} < -30$ dBZ), and their density is multiplied by 0.1. The bin width is 2.5° and 2 dBZ.

precipitating particles are too large. Furthermore, the precipitating mode occurs in the same temperature region between 0 and −10°C as the nonprecipitating mode, instead of being near −15°C as found in observations.

A3. Correspondence of Proposed Cloud Types to CloudSat Level 2 Cloud Scenario

For reference, we compare the newly defined cloud types with those from the official CloudSat Project Level 2 combined radar cloud scenario classification product. Figure A2 shows the frequency of categories of the CloudSat Level 2 cloud scenario category for each newly defined cloud-type pixel in the three latitude bands. (As this version of the cloud scenario product does not use lidar information, the comparison does not include the lidar-only detected cloud types.) Hn mostly corresponds to cirrus (Ci), for all bands. Hp mostly corresponds to altostratus (As) or nimbostratus (Ns) in the Arctic but is more commonly Ci and As over the midlatitude and tropics. Sp corresponds to Ns in the Arctic but deep convection (DC) in the tropics. Ln and Lp mostly correspond to Sc for all bands. Thus, overall, the cloud types with CTT below −28°C or above 0°C are related to one or two categories of cloud scenario, but the other cloud types are more ambiguous.

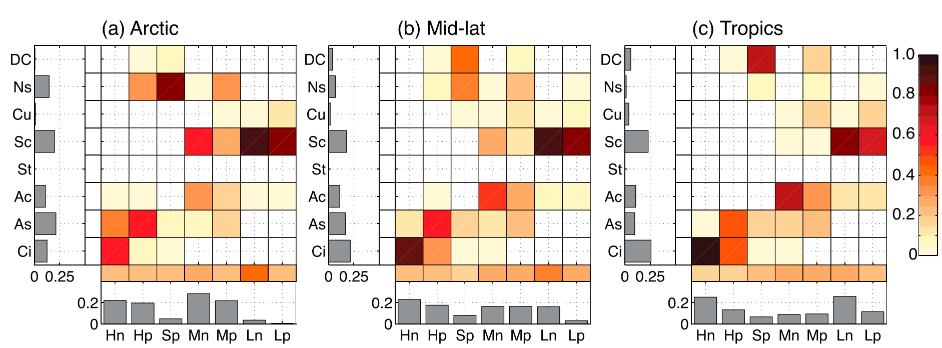

Figure A2. Frequency (color fill) of categories of cloud scenario for a given cloud type over (a) Arctic, (b) midlatitude, and (c) Tropics. The vertical axis shows eight cloud scenario categories: cirrus (Ci), altostratus (As), altocumulus (Ac), stratus (St), stratocumulus (Sc), cumulus (Cu), nimbostratus (Ns), and deep convection (DC). The horizontal axis is the cloud types that contain radar signals. Histograms at bottom show the relative frequency of the cloud layers.

Acknowledgments

The CloudSat-CALIPSO merged data set used for this paper is available upon request from H. Okamoto at Kyushu University (http://atmosp.riam.kyushu-u.ac.jp/cloudsatcalipso). The CERES-MODIS-CALIPSO-CloudSat (CCCM) data set is available at NASA Langley Research Center Atmospheric Science Data Center (https://eosweb.larc.nasa.gov/project/ceres/cccm_table). The data set name is CER-NEWS_CCCM_Aqua-FM3-MODIS-CAL-CS RelB1. The CloudSat Project Level 2 combined radar cloud scenario classification product is available at CloudSat Data Processing Center (http://www.cloudsat.cira.colostate.edu). The data set name is 2B-CLDCLASS. The NICAM 3.5 km mesh simulation data used in this paper is available upon request from M. Satoh at The University of Tokyo. The Joint Simulator for Satellite Sensors is available from JAXA EORC Joint Simulator website (http://www.eorc.jaxa.jp/EARTHCARE/about/jointsimulator.html). This research was supported by the JAXA/EarthCARE 1st Research Announcement. T. Hashino was partially supported by the post doctoral fellowship from Academia Sinica, Taiwan. H. Okamoto and Y. Hagihara were supported by the Ministry of Education, Culture, Sports, Science and Technology of Japan through Grant-in-Aid for Scientific Research (A) 25247078. The NICAM simulations were done using the Earth Simulator at the Japan Agency for Marine-Earth Science and Technology (JAMSTEC). The authors thank P. Yang at Texas A&M University for kindly providing the nonspherical single-scattering database for broadband calculation. T. Hashino is grateful for helpful discussion with B.-J. Sohn at Seoul National University and A. Hamada at The University of Tokyo. Finally, the authors are thankful to the anonymous reviewers for their thorough and critical comments.

References

Allan, R. P., and M. A. Ringer (2003), Inconsistencies between satellite estimates of longwave cloud forcing and dynamical fields from reanalyses, *Geophys. Res. Lett.*, *30*(9), 1491, doi:10.1029/2003GL017019.

Baum, B. A., P. Yang, A. J. Heymsfield, C. G. Schmitt, Y. Xie, A. Bansemer, Y.-X. Hu, and Z. Zhang (2011), Improvements in shortwave bulk scattering and absorption models for the remote sensing of ice clouds, *J. Appl. Meteorol. Climatol.*, *50*, 1037–1056.

Bennartz, R., M. D. Shupe, D. D. Turner, V. P. Walden, K. Steffen, C. J. Cox, M. S. Kulie, N. B. Miller, and C. Pettersen (2013), July 2012 Greenland melt extent enhanced by low-level liquid clouds, *Nature*, *496*, 83–86, doi:10.1038/nature12002.

Cesana, G., J. E. Kay, H. Chepfer, J. M. English, and G. de Boer (2012), Ubiquitous low-level liquid-containing Arctic clouds: New observations and climate model constraints from CALIPSO-GOCCP, *Geophys. Res. Lett.*, *39*, L20804, doi:10.1029/2012GL053385.

Chepfer, H., S. Bony, D. Winker, M. Chiriaco, J.-L. Dufresne, and G. Sèze (2008), Use of CALIPSO lidar observations to evaluate the cloudiness simulated by a climate model, *Geophys. Res. Lett.*, *35*, L15704, doi:10.1029/2008GL034207.

Curry, J. A., W. B. Rossow, D. Randall, and J. L. Schramm (1996), Overview of Arctic cloud and radiation characteristics, *J. Clim.*, *9*, 1731–1764.

de Boer, G., E. Eloranta, and M. Shupe (2009), Arctic mixed-phase stratiform cloud properties from multiple years of surface-based measurements at two high-latitude locations, *J. Atmos. Sci.*, *66*, 2874–2887.

de Boer, G., W. Chapman, J. E. Kay, B. Medeiros, M. D. Shupe, S. Vavrus, and J. Walsh (2012), A characterization of the present-day Arctic atmosphere in CCSM4, *J. Clim.*, *25*, 2676–2695.

Gelsthorpe, R. V., A. Heliere, A. Lefebvre, J. Lemanczyk, E. Mateu, and K. Wallace (2008), EarthCARE and its payload, in *Proceedings of SPIE*, vol. 7152, 715207-1–715207-12, SPIE Digital Library.

Gettelman, A., X. Liu, S. J. Ghan, H. Morrison, S. Park, A. J. Conley, S. A. Klein, J. Boyle, D. L. Mitchell, and J.-L. F. Li (2010), Global simulations of ice nucleation and ice supersaturation with an improved cloud scheme in the Community Atmosphere Model, *J. Geophys. Res.*, *115*, D18216, doi:10.1029/2009JD013797.

Greenwald, T. J., Y.-K. Lee, J. A. Otkin, and T. L'Ecuyer (2010), Evaluation of midlatitude clouds in a large-scale high-resolution simulation using CloudSat observations, *J. Geophys. Res.*, *115*, D19203, doi:10.1029/2009JD013552.

Hagihara, Y., H. Okamoto, and R. Yoshida (2010), Development of a combined CloudSat-CALIPSO cloud mask to show global cloud distribution, *J. Geophys. Res.*, *115*, D00H33, doi:10.1029/2009JD012344.

Hagihara, Y., H. Okamoto, and Z. J. Luo (2014), Joint analysis of cloud top heights from CloudSat and CALIPSO: New insights into cloud top microphysics, *J. Geophys. Res. Atmos.*, *119*, 4087–4106, doi:10.1002/2013JD020919.

Hashino, T., and G. Tripoli (2011), The Spectral Ice Habit Prediction System (SHIPS). Part IV: Box model simulations of habit-dependent aggregation process, *J. Atmos. Sci.*, *68*, 1142–1161.

Hashino, T., M. Satoh, Y. Hagihara, T. Kubota, T. Matsui, T. Nasuno, and H. Okamoto (2013), Evaluating cloud microphysics from NICAM against CloudSat and CALIPSO, *J. Geophys. Res. Atmos.*, *118*, 7273–7292, doi:10.1002/jgrd.50564.

Haynes, J. M., T. S. L'Ecuyer, G. L. Stephens, S. D. Miller, C. Mitrescu, N. B. Wood, and S. Tanelli (2009), Rainfall retrieval over the ocean with spaceborne W-band radar, *J. Geophys. Res.*, *114*, D00A22, doi:10.1029/2008JD009973.

Hirakata, M., H. Okamoto, Y. Hagihara, T. Hayasaka, and R. Oki (2014), Comparison of global and seasonal characteristics of cloud phase and horizontal ice plates derived from CALIPSO with MODIS and ECMWF, *J. Atmos. Oceanic Technol.*, *31*, 2114–2130.

Illingworth, A. J., et al. (2014), The EarthCARE Satellite: The next step forward in global measurements of clouds, aerosols, precipitation and radiation, *Bull. Am. Meteorol. Soc.*, doi:10.1175/BAMS-D-12-00227.1.

Intergovernmental Panel on Climate Change (2013), *Climate Change 2013 The Physical Science Basis*, 1535 pp., Cambridge Univ. Press, Cambridge, U. K., and New York. [Available at http://www.ipcc.ch/.]

Kato, S., S. Sun-Mack, W. F. Miller, F. G. Rose, Y. Chen, P. Minnis, and B. A. Wielicki (2010), Relationships among cloud occurrence frequency, overlap, and effective thickness derived from CALIPSO and CloudSat merged cloud vertical profiles, *J. Geophys. Res.*, *115*, D00H28, doi:10.1029/2009JD012277.

Kato, S., et al. (2011), Improvements of top-of-atmosphere and surface irradiance computations with CALIPSO-, CloudSat-, and MODIS-derived cloud and aerosol properties, *J. Geophys. Res.*, *116*, D19209, doi:10.1029/2011JD016050.

Kato, S., N. G. Loeb, F. G. Rose, D. R. Doelling, D. A. Rutan, T. E. Caldwell, L. Yu, and R. A. Weller (2013), Surface irradiances consistent with CERES-derived top-of-atmosphere shortwave and longwave irradiances, *J. Clim.*, *26*, 2719–2740.

Kay, J., and A. Gettelman (2009), Cloud influence on and response to seasonal Arctic sea ice loss, *J. Geophys. Res.*, *114*, D18204, doi:10.1029/2009JD011773.

Kimura, T., H. Nakatsuka, K. Sato, Y. Sakaide, Y. Seki, K. Okada, N. Takahashi, Y. Ohno, and H. Horie (2010), EarthCARE mission with Japanese Space Borne Doppler Cloud Radar; CPR, paper presented at International Society for Photogrammetry and Remote Sensing (ISPRS) Technical Commission VIII Symposium, Kyoto, Japan.

Kodama, C., A. T. Noda, and M. Satoh (2012), An assessment of the cloud signals simulated by NICAM using ISCCP, CALIPSO, and CloudSat Satellite simulators, *J. Geophys. Res.*, *117*, D12210, doi:10.1029/2011JD017317.

L'Ecuyer, T., and J. H. Jiang (2010), Touring the atmosphere aboard the A-Train, *Phys. Today*, *63*, 36–41, doi:10.1063/1.3463626.

L'Ecuyer, T., N. B. Wood, T. Haladay, G. L. Stephens, and P. W. Stackhouse Jr. (2008), Impact of clouds on atmospheric heating based on the R04 CloudSat fluxes and heating rates data set, *J. Geophys. Res.*, *113*, D00A15, doi:10.1029/2008JD009951.

Li, J., Y. Yi, P. Minnis, J. Huang, H. Yan, Y. Ma, W. Wang, and J. K. Ayers (2011), Radiative effect differences between multi-layered and single-layer clouds derived from CERES, CALIPSO, and CloudSat data, *J. Quant. Spectrosc. Radiat. Transfer*, *112*, 361–375.

Liu, G. (2008), Deriving snow cloud characteristics from CloudSat observations, *J. Geophys. Res.*, *113*, D00A09, doi:10.1029/2007JD009766.

Liu, Z., M. Vaughan, D. Winker, C. Kittaka, B. Getzewich, R. Kuehn, A. Omar, K. Powell, C. Trepte, and C. Hostetler (2009), The CALIPSO lidar cloud and aerosol discrimination: Version 2 algorithm and initial assessment of performance, *J. Atmos. Oceanic Technol.*, *26*, 1198–1213, doi:10.1175/2009JTECHA1229.1.

Loeb, N. G., N. Manalo-Smith, S. Kato, W. F. Miller, S. K. Gupta, P. Minnis, and B. A. Wielicki (2003a), Angular distribution models for top-of-atmosphere radiative flux estimation from the clouds and the Earth's radiant energy system instrument on the Tropical Rainfall Measuring Mission satellite. Part I: Methodology, *J. Appl. Meteorol.*, *42*, 240–265.

Loeb, N. G., K. Loukachine, N. Manalo-Smith, B. A. Wielicki, and D. F. Young (2003b), Angular distribution models for top-of-atmosphere radiative flux estimation from the clouds and the Earth's radiant energy system instrument on the Tropical Rainfall Measuring Mission satellite. Part II: Validation, *J. Appl. Meteorol.*, *42*, 1748–1769.

Masunaga, H., and C. D. Kummerow (2005), Combined radar and radiometer analysis of precipitation profiles for a parametric retrieval algorithm, *J. Atmos. Oceanic Technol.*, *22*, 909–929.

McGill, M. J., M. A. Vaughan, C. R. Trepte, W. D. Hart, D. L. Hlavka, D. M. Winker, and R. Kuehn (2007), Airborne validation of spatial properties measured by the CALIPSO lidar, *J. Geophys. Res.*, *112*, D20201, doi:10.1029/2007JD008768.

Miyamoto, Y., Y. Kajikawa, R. Yoshida, T. Yamaura, H. Yashiro, and H. Tomita (2013), Deep moist atmospheric convection in a subkilometer global simulation, *Geophys. Res. Lett.*, *40*, 4922–4926, doi:10.1002/grl.50944.

Mori, M., M. Watanabe, H. Shiogama, J. Inoue, and M. Kimoto (2014), Robust Arctic sea-ice influence on the frequent Eurasian cold winters in past decades, *Nat. Geosci.*, *7*, 869–873.

Morrison, H., et al. (2011), Intercomparison of cloud model simulations of Arctic mixed-phase boundary layer clouds observed during SHEBA/FIRE-ACE, *J. Adv. Model. Earth Syst.*, *3*, M06003, doi:10.1029/2011MS000066.

Nam, C., S. Bony, J.-L. Dufresne, and H. Chepfer (2012), The 'too few, too bright' tropical low-cloud problem in CMIP5 models, *Geophys. Res. Lett.*, *39*, L21801, doi:10.1029/2012GL053421.

Nishizawa, T., H. Okamoto, T. Takemura, N. Sugimoto, I. Matsui, and A. Shimizu (2008), Aerosol retrieval from two-wavelength backscatter and one-wavelength polarization lidar measurement taken during the MR01K02 cruise of the R/V Mirai and evaluation of a global aerosol transport model, *J. Geophys. Res.*, *113*, D21201, doi:10.1029/2007JD009640.

Okamoto, H., S. Iwasaki, M. Yasui, H. Horie, H. Kuroiwa, and H. Kumagai (2003), An algorithm for retrieval of cloud microphysics using 95-GHz cloud radar and lidar, *J. Geophys. Res.*, *108*, D74226, doi:10.1029/2001JD001225.

Okamoto, H., et al. (2007), Vertical cloud structure observed from shipborne radar and lidar: Mid-latitude case study during the MR01/K02 cruise of the R/V Mirai, *J. Geophys. Res.*, *112*, D08216, doi:10.1029/2006JD007628.

Okamoto, H., T. Nishizawa, T. Takemura, K. Sato, H. Kumagai, Y. Ohno, N. Sugimoto, A. Shimizu, I. Matsui, and T. Nakajima (2008), Vertical cloud properties in the tropical western Pacific Ocean: Validation of the CCSR/NIES/FRCGC GCM by shipborne radar and lidar, *J. Geophys. Res.*, *113*, D24213, doi:10.1029/2008JD009812.

Okamoto, H., K. Sato, and Y. Hagihara (2010), Global analysis of ice microphysics from CloudSat and CALIPSO: Incorporation of specular reflection in lidar signals, *J. Geophys. Res.*, *115*, D22209, doi:10.1029/2009JD013383.

Rossow, W. B., and R. A. Schiffer (1991), ISCCP cloud data products, *Bull. Am. Meteorol. Soc.*, *72*, 2–20.

Sassen, K., and Z. Wang (2008), Classifying clouds around the globe with the CloudSat radar: 1-year of results, *Geophys. Res. Lett.*, *35*, L04805, doi:10.1029/2007GL032591.

Sassen, K., Z. Wang, and D. Liu, (2008), Global distribution of cirrus clouds from CloudSat/Cloud-Aerosol Lidar and Infrared Pathfinder Satellite Observations (CALIPSO) measurements, *J. Geophys. Res.*, *113*, D00A12, doi:10.1029/2008JD009972.

Satoh, M., T. Matsuno, H. Tomita, H. Miura, T. Nasuno, and S. Iga (2008), Nonhydrostatic icosahedaral atmospheric model (NICAM) for global cloud resolving simulations, *J. Comput. Phys.*, *227*, 3486–3514, doi:10.1016/j.jcp2007.02.006.

Satoh, M., et al. (2014), The non-hydrostatic icosahedral atmospheric model: Description and development, *Prog. Earth Planet. Sci.*, *1*, 18, doi:10.1186/s40645-014-0018-1.

Seiki, T., and T. Nakajima (2014), Aerosol effects of the condensation process on a convective cloud simulation, *J. Atmos. Sci.*, *71*, 833–853, doi:10.1175/JAS-D-12-0195.1.

Seiki, T., M. Satoh, H. Tomita, and T. Nakajima (2014), Simultaneous evaluation of ice cloud microphysics and nonsphericity of the cloud optical properties using hydrometeor video sonde and radiometer sonde in situ observations, *J. Geophys. Res. Atmos.*, *119*, 6681–6701, doi:10.1002/2013JD021086.

Sekiguchi, M., and T. Nakajima (2008), A k-distribution-based radiation code and its computational optimization for an atmospheric general circulation model, *J. Quant. Spectrosc. Radiat. Transfer*, *109*, 2779–2793.

Shupe, M., and J. Intrieri (2004), Cloud radiative forcing of the Arctic surface: The influence of cloud properties, surface albedo, and solar zenith angle, *J. Clim.*, *17*, 616–628.

Shupe, M. D., P. Kollias, P. O. G. Persson, and G. M. McFarquhar (2008), Vertical motions in Arctic mixed-phase stratiform clouds, *J. Atmos. Sci.*, *65*, 1304–1322.

Skamarock, W. C., J. B. Klemp, J. Dudhia, D. O. Gill, D. M. Barker, W. Wang, and J. G. Powers (2005), A description of the Advanced Research WRF version 2, *NCAR Tech. Note TN-468 + STR*, 88 pp.

Sohn, B.-J., and R. Bennartz (2008), Contribution of water vapor to observational estimates of longwave cloud radiative forcing, *J. Geophys. Res.*, *113*, D20107, doi:10.1029/2008JD010053.

Sohn, B.-J., T. Nakajima, M. Satoh, and H.-S. Jang (2010), Impact of different definitions of clear-sky flux on the determination of longwave cloud radiative forcing: NICAM simulation results, *Atom. Chem. Phys.*, *10*, 11,641–11,646, doi:10.5194/acp-10-11641-2010.

Stephens, G. L., and N. B. Wood (2007), Properties of tropical convection observed by millimeter-wave radar systems, *Mon. Weather Rev.*, *135*, 821–842.

Su, H., et al. (2013), Diagnosis of regime-dependent cloud simulation errors in CMIP5 models using "A-Train" satellite observations and reanalysis data, *J. Geophys. Res. Atmos.*, *118*, 2762–2780, doi:10.1029/2012JD018575.

Suzuki, K., J.-C. Golaz, and G. L. Stephens (2013), Evaluating cloud tuning in a climate model with satellite observations, *Geophys. Res. Lett.*, *40*, 4464–4468, doi:10.1002/grl.50874.

Takahashi, T., T. Endoh, G. Wakahama, and N. Fukuta (1991), Vapor diffusional growth of free-falling snow crystals between −3 and −23°C, *J. Meteorol. Soc. Jpn.*, *69*, 15–30.

Tomita, H. (2008), New microphysics with five and six categories with diagnostic generation of cloud ice, *J. Meteorol. Soc. Jpn.*, *86A*, 121–142.

Tomita, H., and M. Satoh (2004), A new dynamical framework of nonhydrostatic global model using the icosahedral grid, *Fluid Dyn. Res.*, *34*, 357–400, doi:10.1016/j.fluiddyn.2004.03.003.

Vaughan, M. A., K. A. Powell, R. E. Kuehn, S. A. Young, D. M. Winker, C. A. Hostetler, W. H. Hunt, Z. Liu, M. J. McGill, and B. J. Getzewich (2009), Fully automated detection of cloud and aerosol layers in the CALIPSO lidar measurements, *J. Atmos. Oceanic Technol.*, *26*, 2034–2050, doi:10.1175/2009JTECHA1228.1.

Wang, J., and B. Geerts (2003), Identifying drizzle within marine stratus with W-band radar reflectivity, *Atmos. Res.*, *69*, 1–27.

Webb, M., C. Senior, S. Bony, and J.-J. Morerette (2001), Combining ERBE and ISCCP data to assess clouds in the Hadley Centre, ECMWF and LMD atmospheric climate models, *Clim. Dyn.*, *17*, 905–922.

Wielicki, B. A., B. R. Barkstrom, E. F. Harrison, R. B. Lee III, G. L. Smith, and J. E. Cooper (1996), Clouds and the Earth's Radiant Energy System (CERES): An Earth observing system experiment, *Bull. Am. Meteorol. Soc.*, *77*, 853–868.

Yang, P., L. Bi, B. A. Baum, K.-N. Liou, G. W. Kattawar, M. I. Mishchenko, and B. Cole (2013), Spectrally consistent scattering, absorption, and polarization properties of atmospheric ice crystals at wavelengths from 0.2 to 100 μm, *J. Atmos. Sci.*, *70*, 330–347.

Yoshida, R., H. Okamoto, Y. Hagihara, and H. Ishimoto (2010), Global analysis of cloud phase and ice crystal orientation from cloud-aerosol lidar and infrared pathfinder satellite observation (CALIPSO) data using attenuated backscattering and depolarization ratio, *J. Geophys. Res.*, *115*, D00H32, doi:10.1029/2009JD012334.

Zhang, Y., S. A. Klein, J. Boyle, and G. G. Mace (2010), Evaluation of tropical cloud and precipitation statistics of Community Atmosphere Model version 3 using CloudSat and CALIPSO data, *J. Geophys. Res.*, *115*, D12205, doi:10.1029/2009JD012006.